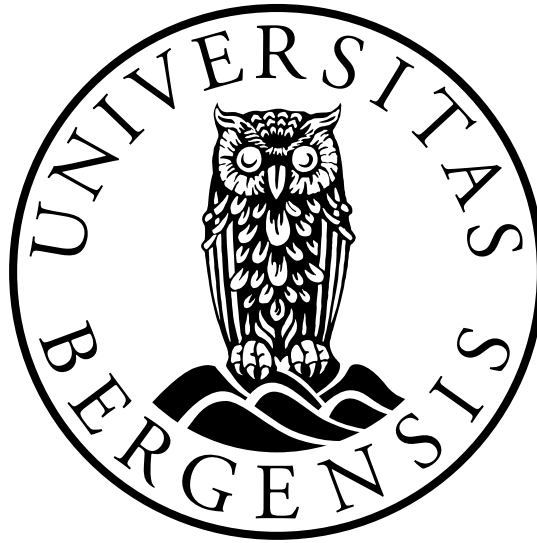UNIVERSITY OF BERGEN

Department of Physics and Technology Studies

MASTER'S THESIS

Microstructure of Charged Particle Tracks Measured with the ALPIDE Pixel Sensor

Author: Ingrid Marie Stuen

December 15, 2021

Abstract

Proton CT has the potential to reduce range uncertainties in particle therapy planning. Proton CT gives a direct three-dimensional map of the stopping power of the tissue. This lowers the range uncertainties compared to conventional CT that requires a conversion from Hounsfield units to stopping power.

The Bergen pCT collaboration is constructing a pCT prototype based on a high granularity digital tracking calorimeter. The high granularity is achieved using the ALPIDE sensor, which is a monolithic active pixel sensor. The ALPIDE sensor was developed for the ALICE experiment at CERN.

In this thesis, experimental data from different setups with ALPIDE chips is analysed, with the goal of characterising the ALPIDE for use in the Bergen pCT prototype. The impact of different configuration parameters on the charge threshold and noise level of the ALPIDE, as well as the impact of charge threshold on cluster formation, are investigated to see how these parameters can be optimised for the pCT system.

The microstructure of charged particle tracks in the ALPIDE is studied to see how the particles interact with the detector material on a micrometre scale. Long track structures in the sensitive layers of an electromagnetic calorimeter are studied, and associated energy spectra are compared to δ-electron spectra. Finally, lateral scans of ion beams are used to study the microstructure of helium and carbon ion tracks in an ALPIDE chip.

Acknowledgment

First of all, I would like to thank my supervisor, professor Dieter Röhrich. Thank you, Dieter, for providing me with an interesting project and for all your guidance along the way. A big thank you to PhD candidate Viljar Nilsen Eikeland for all your help throughout this process. It has been a pleasure to be a part of the Bergen pCT collaboration.

I would also like to thank all my friends and fellow students at the department for all the good times we have shared. Thank you, Lena and Minh Chi, who have stuck with me from the very start, Isabel and Andreas for motivating me and giving me chocolate, and all other friends, you know who you are. A special thanks to my dear friend and trusty study partner, Emilie. I am forever grateful for having you in my (study) life.

Finally, a big thank you to my family for all their unconditional love and support. Special thanks to my parents for always being there for me and making my life a little easier in any way they can.

Contents

List of Figures

List of Tables

List of abbreviations

ALICE A Large Ion Collider Experiment

ALPIDE ALICE Pixel Detector

CMOS Complementary Metal-Oxide Semiconductor

CPU Central Processing Unit

CSDA Continuously Slowing Down Approximation

CT Computed Tomography

DAQ Data Acquisition

DECT Dual Energy Computed Tomography

DESY Deutsches Elektronen-Synchotron

DTC Digital Tracking Calorimeter

FHR Fake-Hit Rate

FROMU Framing and Management Unit

HIT Heidelberg Ion-Beam Therapy Center

HU Hounsfield Units

IMPT Intensity-Modulated Proton Therapy

ITS Inner Tracking System

LET Linear Energy Transfer

LHC Large Hadron Collider

MAPS Monolithic Active Pixel Sensors

MEB Multi Event Buffer

MCS Multiple Coulomb Scattering

pCT proton Computed Tomography

pRU pCT Readout Unit

PSPT Passively Scattered Proton Therapy

RBE Relative Biological Effectiveness

RRU Region Readout Unit

RSP Relative Stopping Power

SOBP Spread Out Bragg Peak

TRU Top Readout Unit

Chapter 1

Introduction

The goal of radiotherapy is to deliver a homogenous radiation dose to a tumour inside the patient whilst minimising the dose to healthy tissue. Most of the current practice of clinical radiotherapy utilises photon beams, but the use of proton and carbon ion beams is increasing. In particle therapy the characteristic depth-dose curve of charged particles are exploited to deliver a high dose to the treatment volume while reducing the dose delivered to healthy tissue.

Treatment planning for particle therapy requires an accurate map of the relative stopping power (RSP) of the tissue. This is currently done by using x-ray CT images and converting Hounsfield units to RSP, giving an uncertainty of about 3.5% in the RSP estimation. Proton CT can be used to directly reconstruct 3D maps of RSP values, reducing the range uncertainties.

The Bergen pCT collaboration aims to design and build a pCT prototype with a high granularity digital tracking calorimeter used as both tracking and energy/range detector.

1.1   About this Thesis

The main objective of this thesis is to characterise the ALPIDE chip for use in the Bergen pCT system.

Experiments were conducted at the University of Bergen to study how different factors affect the charge threshold of the ALPIDE and how the threshold affects cluster sizes. The aim is to optimise the ALPIDE configuration parameters for proton tracks.

Data from beam tests with the ALPIDE sensor was used to study the microstructure of charged particle tracks. This can be used to get exact descriptions of how charged particles deposit

energy and be used to make radiobiological predictions.

1.2   Thesis Outline

Chapter 2: Ionising radiation and radiation therapy This chapter introduces ionising radiation and some medical applications. It describes how photons and charged particles interact with matter and deposit dose and how this is used in radiotherapy treatment. The basic concept behind proton CT is introduced.

Chapter 3: Silicon Pixel Sensor - ALPIDE This chapter describes the basic properties of pixel detectors. It also introduces Monolithic Active Pixel Sensors and cluster formation. The general architecture and operations of the ALICE pixel detector is introduced. Finally, the conceptual design of the Bergen pCT prototype is described.

Chapter 4: Optimisation of ALPIDE's configuration parameters In this chapter the effect of charge threshold on cluster formation and noise is studied with an Am-241 source. How some analog front-end settings affect the charge threshold and fake-hit rate is investigated. Some calculations are performed to see how masking can reduce the data-rate from noise in the final pCT system.

Chapter 5: Characterisation of the ALPIDE with Electron and Carbon Ion Tracks In this chapter microstructures of charged particle tracks are studied. First, the length of tracks in the sensitive layers of an electromagnetic calorimeter irradiated by an electron beam are analysed. The microstructure of carbon and helium tracks is investigated through analysis of lateral beam scans with a single ALPIDE chip.

Chapter 6: Conclusion This chapter summarises the findings from chapter 4 and 5.

1.3   Citation Principles

Citations placed after a punctuation refers to several statements while citations placed before a punctuation refers only to that specific statement.

Chapter 2

Ionising radiation and radiation therapy

2.1 Photon Interactions with Matter

Electromagnetic waves with large enough energy to ionise atoms and molecules can be described as a stream of particles, the photons. The energy of each photon is $h\nu$, where h is Planck's constant and ν is the frequency. [1]

Photons travelling through an absorbing medium may experience various interactions with the nuclei or orbital electrons in the medium. Photon interactions are stochastic by nature, and photons may undergo a few, one, or no interactions as they pass through matter[1]. The main interactions are

- Photoelectric effect

- Compton scattering

- Pair production

In these interactions, photons are either absorbed or scattered. If a monoenergetic photon beam with initial intensity I_0 passes through a medium, the interactions result in a loss of intensity. The intensity of the beam after traversing an absorber of thickness x is given by

$$I(x) = I_0 e^{-\mu x} \tag{2.1}$$

where μ is the linear attenuation coefficient. This coefficient can be described as the probability per unit path length that a photon will have an interaction with the absorber. [2] It is characteristic of the absorbing material and is directly related to the total interaction cross-

section σ_{tot} [3]. The total interaction cross-section is the sum of the cross-sections for the individual processes

$$\sigma_{tot} \approx \sigma_{pe} + \sigma_c + \sigma_{pp} \tag{2.2}$$

where σ_{pe}, σ_c and σ_{pp} are the cross-sections for photoelectric effect, Compton scattering and pair production, respectively. [1]

2.1.1   Photoelectric Effect

In the photoelectric effect, a photon is absorbed by an atomic electron. The electron is subsequently ejected from the atom with a kinetic energy

$$E_K = h\nu - E_B \tag{2.3}$$

where $h\nu$ is the photon's energy and E_B is the binding energy of the atomic electron. For momentum to be conserved when the photon is absorbed, the nucleus must absorb the recoil momentum. The photoelectric effect, therefore, only occurs with bound electrons. [3]

In general, the cross-section for the photoelectric effect increases with decreasing photon energy. The photoelectric effect is the dominant mode of interaction of photons with energy lower than 100 keV. The energy dependence of the cross-section is approximately given by

$$\sigma_{pe} \propto \frac{Z^n}{(h\nu)^{3.5}} \tag{2.4}$$

where Z is the charge of the nucleus, the coefficient n varies between 4 and 5. [4]

2.1.2   Compton Scattering

In Compton scattering, a photon scatters on a free electron. An electron can be considered free when the electron's binding energy is much smaller than the energy of the incoming photon. [3] A sketch of the collision can be seen in Figure 2.1.
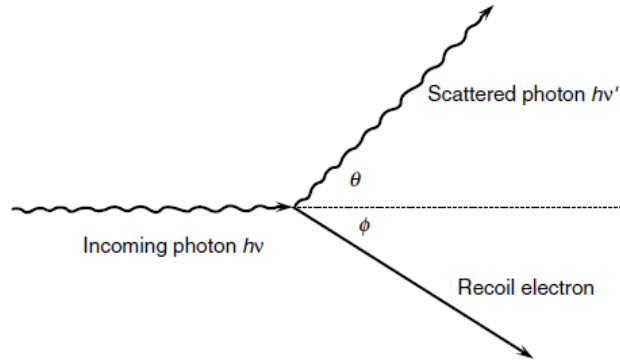
Figure 2.1: Kinematics of Compton scattering [1]

The energies of the photon and electron after the collision can be calculated using the conservation of energy and momentum. The energy of the photon is given by

$$hv' = \frac{hv}{1 + \gamma(1 - \cos\theta)} \tag{2.5}$$

and the kinetic energy of the electron is given by

$$E_k = hv - hv' = \frac{\gamma(1 - \cos\theta)}{1 + \gamma(1 - \cos\theta)} \tag{2.6}$$

where $\gamma = hv/m_e c^2$. [3]

Compton scattering is the dominant interaction for photon energies in the range 100 keV - 1 MeV. [4] The cross-section for Compton scattering can be calculated using the Klein-Nishina formula

$$\frac{d\sigma_c}{d\Omega} = \frac{r_e^2}{2} \frac{1}{[1 + \gamma(1 - \cos\theta)]^2} \left(1 + \cos^2\theta + \frac{\gamma^2(1 - \cos\theta)^2}{1 + \gamma(1 - \cos\theta)}\right) \tag{2.7}$$

where r_e is the classical electron radius. The total probability per electron for a Compton scattering to occur is found by integrating this formula over $d\Omega$

$$\sigma_c = 2\pi r_e^2 \left(\frac{1 + \gamma}{\gamma^2} \left[\frac{2(1 + \gamma)}{1 + 2\gamma} - \frac{1}{\gamma} ln(1 + 2\gamma)\right] + \frac{1}{2\gamma} ln(1 + 2\gamma) - \frac{1 + 3\gamma}{(1 + 2\gamma)^2}\right) \tag{2.8}$$

The maximum energy that can be transferred to the electron is given by

$$E_{k,max} = hv \left(\frac{2\gamma}{1 + 2\gamma}\right) \tag{2.9}$$

and is called the Compton edge. [3]

2.1.3   Pair Production

Pair production is possible when photons with energy larger than 1.022 MeV interact with matter. The process involves the transformation of a photon into an electron-positron pair. This can only occur near a third body, usually a nucleus, to conserve momentum. [3] Because the rest mass of an electron is 511 keV, 1.022 MeV is the threshold value for pair production to occur. If the photon energy is higher than this threshold value, the excess energy is divided as kinetic energy between the electron and the positron. [5]

The cross-section for pair production in the nuclear field is zero below the threshold. It then rapidly increases with increasing energy and, well above the threshold, the Z dependency is approximately $\sigma_{pp} \propto Z^2$. [1]

2.2   Charged Particle Interactions with Matter

Charged particles with initial kinetic energy moving through matter will transfer energy to the matter through various interactions. The Coulomb electric field that surrounds the charged particle will interact with orbital electrons and the nucleus of all atoms it encounters as it moves through the matter [2]. This leads to energy loss and deflection of the charged particle. Some of the possible interactions are:

- inelastic collisions with atomic electrons

- elastic collisions with nuclei

- emission of Cherenkov radiation

- nuclear reactions

- bremsstrahlung

While collisions between the particle and atomic electrons and nuclei frequently occur as the particle travels through matter, the other interactions are quite rare. [3] In the following, the energy loss for particles heavier than the electron and the energy loss for electrons and positrons will be treated separately.

2.2.1   Energy loss of heavy charged particles

The inelastic collisions with atomic electrons are almost solely responsible for the energy loss of heavy particles. In these collisions, the charged particle transfers a small fraction of its

kinetic energy to the atom causing excitation or ionisation. Although the energy transfer in each collision is minimal, the number of collisions per unit length in normally dense matter is so high that there is a substantial cumulative energy loss. [3]

These collisions can be categorised as soft or hard collisions. In a soft collision, only an excitation happens. In a hard collision, the energy transfer is large enough to cause ionisation. If the energy transfer in a hard collision is large enough, the ejected electron can cause substantial secondary ionisation. These high-energy electrons are referred to as δ-rays or δ-electrons. [3]

Inelastic collisions are statistical in nature and occur with a certain quantum mechanic probability. However, because the number of collisions per unit path length is large, the fluctuations in the total energy loss are small, and one can meaningfully work with the average energy loss per unit path length. The average energy loss per unit path length, $-dE/dx$, is often referred to as the stopping power and can be calculated using the Bethe-Bloch formula. The Bethe-Bloch formula, with density effect and shell corrections, is shown in equation 2.10. [3]

$$-\frac{dE}{dx} = 2\pi N_a r_e^2 m_e c^2 \rho \frac{Z}{A} \frac{z^2}{\beta^2} \left[ln\left(\frac{2m_e\gamma^2 v^2 W_{max}}{I^2}\right) - 2\beta^2 - \delta - 2\frac{C}{Z} \right] \tag{2.10}$$

The parameters of equation 2.10 are listed below.

$$2\pi N_a r_e^2 m_e c^2 = 0.1535 MeV cm^2/g$$

r_e: classical electron radius $= 2.817 \times 10^{-13}$cm

m_e: electron mass

N_a: Avogadro's number $= 6.022 \times 10^{23}$mol^{-1}

I: mean excitation potential

Z: atomic number of absorbing material

A: atomic weight of absorbing material

ρ: density of absorbing material

z: charge of incident particle in units of e

$\beta =$ v/c of the incident particle

$\gamma =$ $1/\sqrt{1-\beta^2}$

δ: density correction

C: shell correction

W_{max}: maximum energy transfer in a single collision

The maximum energy transfer in a single collision for an incident particle with mass M is:

$$W_{max} = \frac{2m_e c^2 \eta^2}{1 + 2s\sqrt{1 + \eta^2} + s^2} \tag{2.11}$$

where $s = m_e/M$ and $\eta = \beta\gamma$.

The shell correction, C, is added to correct for the assumption that the velocity of the heavy charged particle is much larger than that of the orbital electrons in the matter. This assumption does not hold at low energies. When the velocity of the orbital electrons becomes comparable to that of the heavy charged particle, it stops participating in energy transfer from the charged particle. This effect causes an overestimate of the mean excitation potential, I, and in turn, underestimates the stopping power at low energies. [2]

The density correction, δ, corrects for the effect arising from the electric field of the particle polarising the atoms along its path. Because of this polarisation, electrons far from the particle's path will be shielded from the full electric field intensity. This effect results in an overestimate in stopping power at high energies. [3]

Figure 2.2 shows the energy loss of positive muons on a copper target over a wide range of incident momenta.
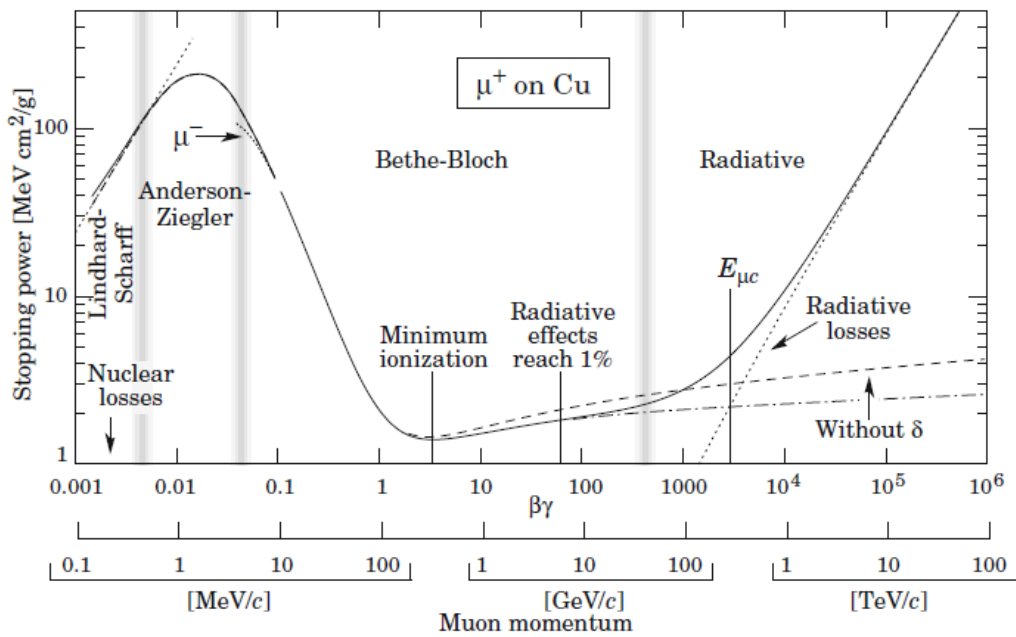
Figure 2.2: Mean energy loss for positive muons incident onto a Cu target, as predicted by the Bethe- Block formula and its modifications [6]

2.2.2 Energy loss of light charged particles

Like heavy charged particles, electrons and positrons lose energy through collisions. However, due to their small mass, the emission of electromagnetic radiation from scattering in

the electric field of a nucleus (bremsstrahlung). This process is a relatively minor factor at energies below a few MeV. With increasing energies, the probability of bremsstrahlung rises rapidly. At energies above a few 10's of MeV, energy loss by radiation is comparable to or greater than energy loss from collisions. The stopping power of electrons and positrons is therefore composed of two separate parts:

$$\left(\frac{dE}{dx}\right)_{tot} = \left(\frac{dE}{dx}\right)_{rad} + \left(\frac{dE}{dx}\right)_{coll} \tag{2.12}$$

The probability of emission of bremsstrahlung radiation varies as the inverse square of the particle mass. At energies below a few hundred GeV, electrons and positrons are the only particles with substantial energy loss due to bremsstrahlung. Since bremsstrahlung emission depends on the strength of the electric field felt by the electron, the amount of screening from the atomic electrons surrounding the nucleus also affects the cross-section. [3]

The basic mechanisms of collision loss as described for heavy charged particles also hold for electrons and positrons. However, the Bethe-Bloch formula must be modified. Firstly the assumption that the incident particle remains undeflected during the collision process does not hold due to the low mass. Secondly, for electrons, the collisions are between identical particles, so that the calculation must take into account their indistinguishability. Several terms in the formula are changed due to these considerations. In particular, the maximum energy transfer in a single collision becomes $W_{max} = T_e/2$, where T_e is the kinetic energy of the incident particle. The modified Bethe-Bloch formula becomes

$$-\frac{dE}{dx} = 2\pi N_a r_e^2 m_e c^2 \rho \frac{Z}{A} \frac{1}{\beta^2} \left[ln\left(\frac{\tau^2(\tau+2)}{2(I/m_e c^2)^2}\right) + F(\tau) - \delta - 2\frac{C}{Z} \right] \tag{2.13}$$

where τ is the kinetic energy of the particle in units of $m_e c^2$ and

$$F(\tau) = \begin{cases} 1 - \beta^2 + \frac{\tau^2/8 - (2r+1)ln2}{(\tau+1)^2} & \text{for } e^- \\ 2ln2 - \frac{\beta^2}{12}\left(23 + \frac{14}{\tau+2} + \frac{10}{(\tau+2)^2} + \frac{4}{(\tau+2)^3}\right) & \text{for } e^+ \end{cases} \tag{2.14}$$

The rest of the quantities are as defined in section 2.2.1. [3]

Figure 2.3 illustrates the contributions of radiation and collision losses to the total energy loss for electrons.
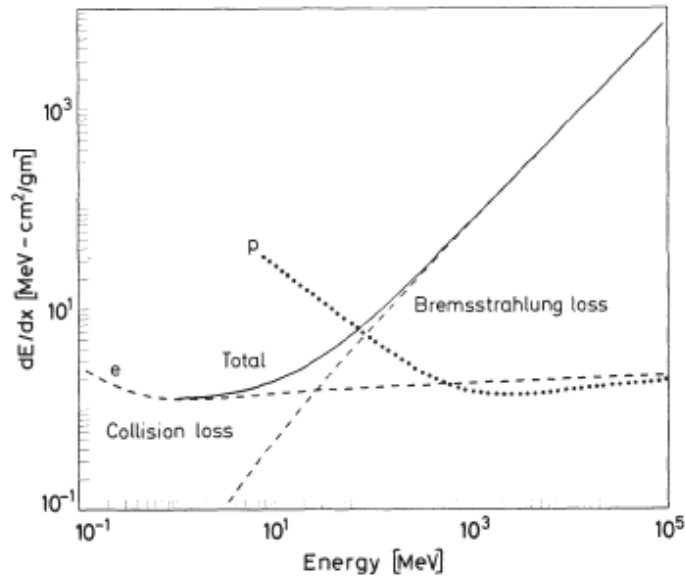
Figure 2.3: Energy loss of electrons in copper, with dE/dx for protons for comparison. [3]

2.2.3 Electromagnetic Showers and Calorimeters

Energetic electrons, positrons or photons passing through matter can initiate a chain of interactions making an electromagnetic shower. Electrons and positrons at high energies are likely to interact with matter through bremsstrahlung radiation, producing photons. The photons can, in turn, produce electrons and positrons through pair production. The number of particles grows progressively through these processes and an electromagnetic shower is formed as illustrated in Figure 2.4. The shower will stop once the energy of the secondary photons is no longer sufficient to produce electron-positron pairs. The penetration depth of the electromagnetic shower is directly related to the initial energy of the particle that initiated the shower. [6]
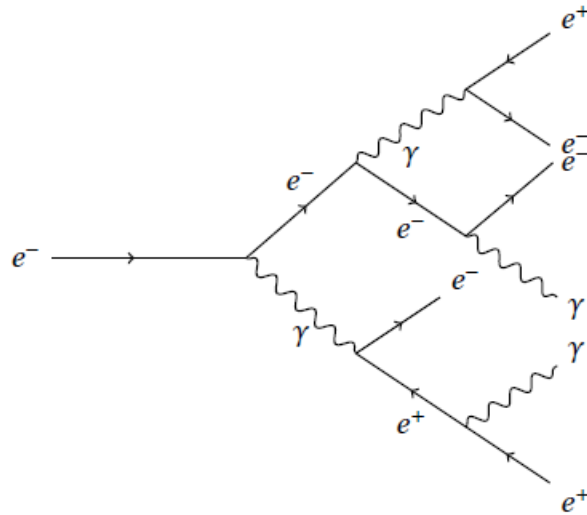
Figure 2.4: Diagram of electromagnetic shower initiated by an electron [7]

Calorimeters are detectors designed to measure energy through total absorption of particles. Electromagnetic calorimeters use the characteristics of electromagnetic showers. The signal produced from energy deposition in the detector volume is proportional to the total deposited energy. Determining the proportionality constant(s) is part of the calibration of the detector. The deposited energy E is in general proportional to the number of interactions n in the detector volume

$$E \propto n \tag{2.15}$$

As in a Poisson process, the width of the deposited energy σ_E is

$$\sigma_E \propto \sqrt{n} \tag{2.16}$$

Combining equations 2.15 and 2.16 gives

$$\frac{\sigma_E}{E} \sim \frac{\sqrt{n}}{n} = \frac{1}{\sqrt{n}} \sim \frac{1}{\sqrt{E}} \tag{2.17}$$

This shows that the energy resolution of a calorimeter improves with higher energies. [6]

In terms of technology and design, there are two classes of electromagnetic calorimeters: homogeneous and sampling. In homogeneous calorimeters, the whole detector volume is filled by a high-density material working as both absorber and sensing medium. Sampling calorimeters, also called sandwich calorimeters, are constructed of alternating layers of absorber and sensing material. While homogeneous calorimeters usually give better resolu-

tion, sampling calorimeters can be made very compact and are generally less expensive. [6]

The energy resolution can be accurately parametrised with three terms

$$\frac{d\sigma_E}{E} = \frac{a}{\sqrt{E}} \oplus \frac{b}{E} \oplus c \tag{2.18}$$

where a, b, and c are constants and the $\oplus$ symbol indicates a sum in quadrature. The three terms are due to energy fluctuations, electronics noise and shower leakage, respectively. [6]

2.2.4 δ-electrons

The energy spectrum of δ-electrons ejected in collisions between an ion and target-atom electrons can be approximated by theoretical models. The differential cross section for an ion with energy E_i and effective charge Z_{eff} to transfer energy E to the ejected electron from the n shell can be approximated by

$$\frac{d\sigma}{dE} = \frac{2\pi e^4 Z_t Z_{eff}^2}{m_0 c^2 \beta^2 E^2} \left[1 - \frac{\beta^2 E}{E_{max}} + \frac{\pi \beta Z_{eff}^2}{137} \left(\frac{E}{E_{max}} \right)^{1/2} \left(1 - \frac{E}{E_{max}} \right) \right] \tag{2.19}$$

where β is the ion velocity in units of light velocity, m_0 is the electron mass, Z_t is the nuclear charge of the target atom, and E_{max} is the maximal energy transferred to the δ-electron in an ion–electron collision. The energy transfer E is the sum of the kinetic energy transferred to the δ-electron E_δ and the binding energy of the electron E_{bn}. Examples of calculated energy spectra of δ-electrons can be seen in Figure 2.5. Eq. (1) in the figure corresponds to equation 2.19 [8]
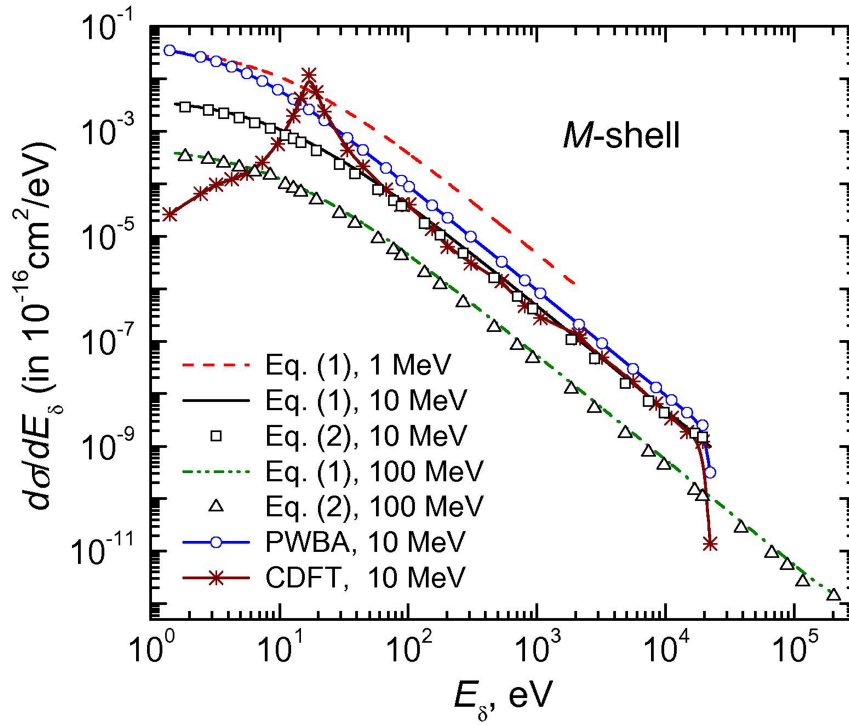
Figure 2.5: Energy spectra for δ-electrons by protons from the silicon M-shell. [8]

The angle θ between the direction of the incident particle and that of the ejected electron is given by $\theta = cos^{-1}(E_\delta/E_{\delta max})^{1/2}$. $\theta \approx \pi/2$ unless E_δ is close to $E_{\delta max}$. [8]

2.2.5 Multiple Coulomb Scattering

Charged particles passing through matter can experience repeated elastic collisions (Coulomb scattering) with nuclei which will deflect the original direction of motion. The individual collisions are governed by the Rutherford formula and mainly result in small angular deflections. For multiple repeated collisions this phenomenon is called multiple Coulomb scattering (MCS). [6]

Figure 2.6 shows a sketch of a particle undergoing MCS in a medium of thickness x. After the particle has undergone MCS, it emerges from the medium at distance y and angle θ from its original trajectory.
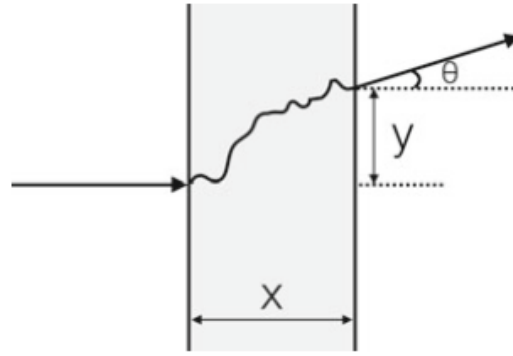
Figure 2.6: Sketch of a particle entering a medium of thickness x and undergoing multiple Coulomb scattering and emerging at a distance y and with angle θ with respect to the original trajectory [6]

For small angles, θ is a random variable described approximately by a Gaussian distribution with width given by the following empirical formula

$$\Delta\theta = \frac{13.6\text{MeV}}{\beta c p} z \sqrt{\frac{z}{X_0}} \left[1 + 0.038 \ln \frac{x}{X_0} \right] \tag{2.20}$$

where z is the charge number of the incident particle, βc and p are its speed and momentum, respectively, and X_0 is the radiation length. [6]

The deflection can be described as follows: [6]

$$\Delta y = \frac{x}{\sqrt{3}} \Delta\theta \tag{2.21}$$

2.2.6   Range and Straggling

The range of a charged particle in a given absorbing medium is an experimental concept providing the thickness of an absorber that the particle can just penetrate. The range depends on both the particle type and the composition of the absorbing material. [2] Charged particles lose energy in a quasi-continuous fashion along their tracks in matter, eventually coming to rest. [1] Mathematically it is convenient to define the so-called continuously-slowing-down-approximation (CSDA) range R_{CSDA} for a particle with initial kinetic energy T_0 as follows:

$$R_{CSDA} = \int_0^{T_0} \left(\frac{dE}{dx} \right)^{-1} dE \tag{2.22}$$

This yields the approximate path length travelled. It does, however, ignore the effect of multi-

ple Coulomb scattering. The range, defined as the straight-line thickness, will thus generally be smaller than the total path length. [3] The effect of multiple Coulomb scattering is small for heavy charged particles, making the CSDA range a good approximation for the average range. The CSDA range can be up to twice the average range for light charged particles that are much more affected by multiple Coulomb scattering. [3, 2]

The stopping power is an average value for the energy loss per unit distance. However, there will be fluctuations about this mean value in real situations. This spread in energy is called energy straggling. [1] This, in turn, gives rise to what is known as range straggling. The effect of this can be seen in Figure 2.7. The distribution in range is approximately Gaussian in form. [3]
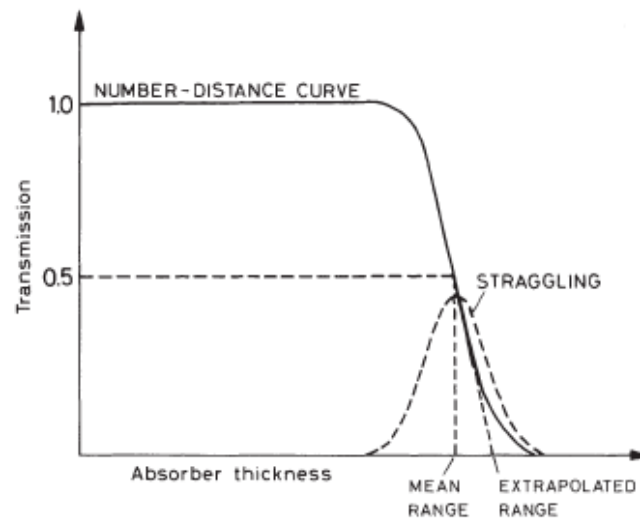
Figure 2.7: Typical range number-distance curve [3]

2.2.7   Bragg Peak

For heavy charged particles, the rate of energy loss per distance travelled is approximately constant and slowly varying over a large range of momenta. In Figure 2.2 this can be seen for $\beta\gamma$ between approximately 3 and 1000. For a proton, this corresponds to momenta between approximately 2.8 and 1000 GeV/c. At $\beta\gamma$ below 3, the energy loss rate increases rapidly. For a beam of heavy charged particles, this implies that most of the energy loss happens in the kinematic range below the minimum ionising point. The distribution of energy loss as a function of penetration depth is therefor approximately constant until the momentum is degraded to $\beta\gamma < 1$, at which point there is a peak in energy deposition. This is called a Bragg curve, and the peak in energy deposition is called a Bragg peak. [6]

Figure 2.8 shows the Bragg curve for 70 MeV protons in water.
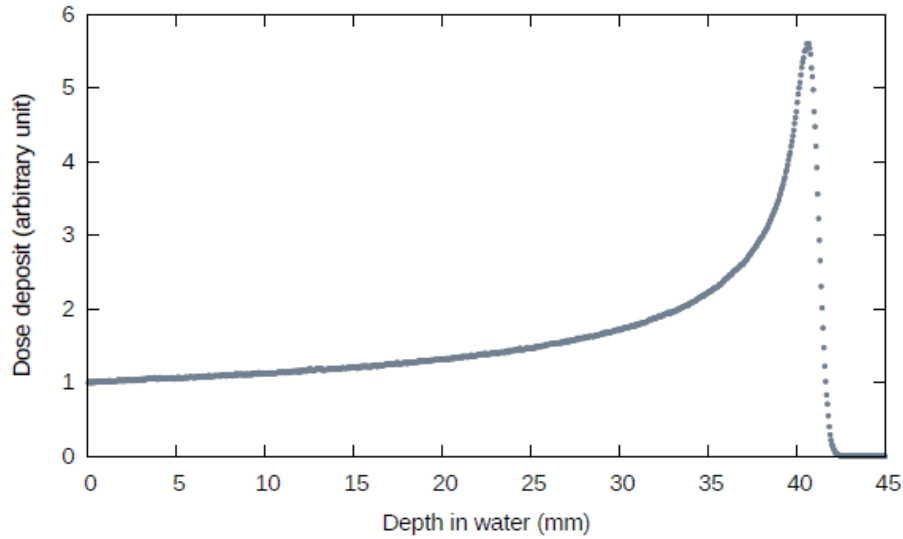
Figure 2.8: Simulated dose deposit of 70 MeV protons in water, normalised to the entrance dose [9]

2.3   Microdosimetry

Radiation damage depends on the absorption of energy from the radiation and is approximately proportional to the mean concentration of absorbed energy in irradiated tissue. The basic unit of radiation dose is therefore expressed in terms of absorbed energy per unit mass of tissue

$$D = \frac{dE}{dm} \tag{2.23}$$

The SI unit for radiation absorbed dose is gray (Gy). One gray corresponds to an absorbed radiation dose of one joule per kilogram. [10]

The ionisation density produced by ionising radiation in tissue depends on the ionising radiation beam's linear energy transfer (LET). The LET is the mean amount of energy that a given ionising radiation imparts to the absorbing medium per unit path length and is used to specify the quality of an ionising radiation beam. [2]

LET is measured in keV/μm. Ionising radiation is categorised as high LET if the LET is above 10 keV/μm and low LET below this value. Heavy charged particles are high LET, photons are low LET, and electrons can be both depending on the electron's energy. The ability of the radiation to produce biological damage increases with increasing LET. [2]

The relative biological effectiveness (RBE) is used to compare the dose of test radiation to the dose of standard radiation to produce the same biological effect. The RBE varies not

only with the type of radiation but also with the type of cell or tissue, the biologic effect under investigation, dose, dose rate and fractionation. In general, the RBE increases with LET to reach a maximum of 3–8 at a very high LET of ~200 keV/μm and then it decreases with further increase in LET. [2]

Although LET gives a good representation of the radiation quality, it might be too simplistic as it is assumed that it is the energy deposition and not the energy loss of a particle that leads to a biological effect. The position of energy loss is not necessarily the same as the position of the energy deposition. This is due to secondary charged particles, typically δ-electrons, that deposit energy at a distance from the position of energy loss. [11]

Microdosimetry was developed to overcome the shortcomings of the LET as a quantity for radiation quality. Microdosimetry studies the distribution of the single energy depositions in space and time. It assumes that the biological effects stem from this pattern of energy depositions and that it is irrelevant what particles produced the pattern. [11]

Structural microdosimetry is an approach that studies the microscopic patterns of energy deposition along the particle tracks. This accurately describes how charged particles deposit energy and may offer better radiobiological predictions. As these microscopic patterns are difficult to measure, structural microdosimetry is mainly a theoretical approach. [11]

2.4   Radiotherapy

The goal of radiotherapy is to deliver a homogeneous radiation dose to a tumour inside the patient whilst minimising the dose to healthy tissue, especially organs that are radiosensitive or close to the tumour. Three-dimensional patient images, usually CT scans, are needed to get detailed information on the tumour's location, size, and shape and radiosensitive organs at risk. The various structures are outlined on a series of axial slices to produce three-dimensional volumes. A radiotherapy plan can then be designed using a detailed computer model of how radiation dose will be deposited within the patient. [12]
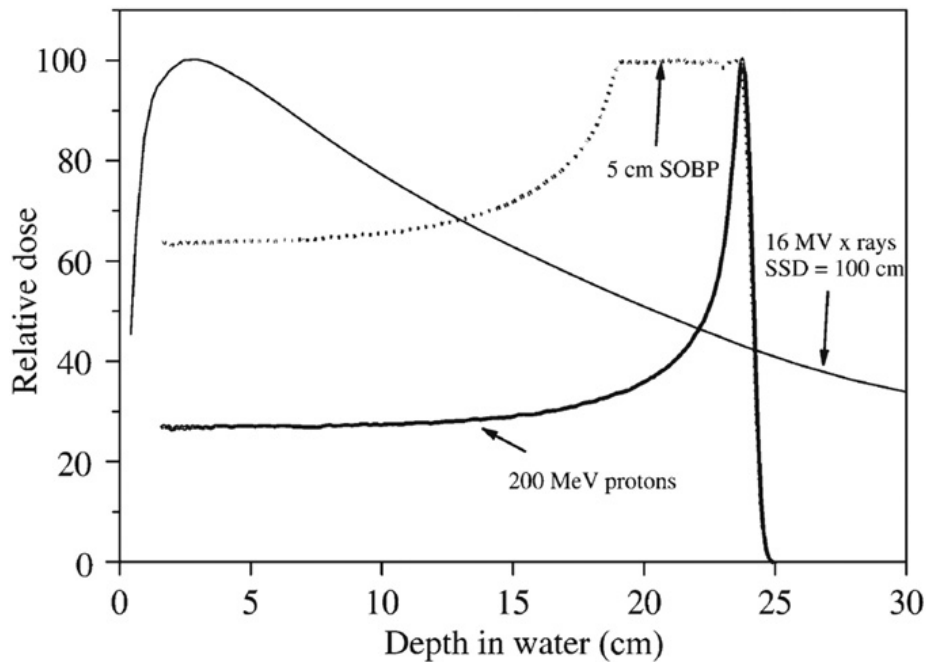
Figure 2.9: Depth-dose curves for 200 MeV protons (monoenergetic and with a 5 cm SOBP) and 16 MV photon beam [13]

Most of the current practice of clinical radiotherapy utilises photon beams of energies ranging from 4 to 18 MV. Photon radiation dose as a function of depth in the patient rises initially as the electrons ejected by photons build up to a maximum and then declines exponentially as photons are absorbed, as seen in Figure 2.9. [13]

Protons lose most of their energy through interactions with electrons. Secondary electrons (δ-electrons) travel a very short distance from the path of the proton ionising and depositing energy. The dose deposition of a monoenergetic proton beam follows the characteristic Bragg curve. This characteristic depth-dose curve can be exploited to reduce the dose to normal tissue. [13]

In proton therapy, protons are accelerated up to therapeutic energies of 70 to 250 MeV in a cyclotron or synchrotron and transported to the treatment room, where they enter the treatment head mounted on a rotating gantry. The beam is spread longitudinally to create a spread-out Bragg peak (SOBP), as seen in Figure 2.9. It is also spread laterally and shaped to conform the high dose regions to the target volume. The two main approaches to shaping the beam are passively scattered proton therapy (PSPT) and intensity-modulated proton therapy (IMPT). In IMPT, thin pencil beams with a sequence of initial energies are magnetically scanned to cover the treatment volume. Each initial energy then covers one layer in the volume. [13]

Protons are assumed to have similar biological effects as photons. Based on numerous in-vitro and animal experiments, protons have been assumed to have a 10% higher biological

effectiveness relative to photons. Thus, an RBE of 1.1 is typically used in clinical practice. [13] For carbon ions the uncertainty in RBE is much larger and can range from 1.3 to 5 [14].

2.5   Imaging Modalities

When using charged particles in treatment, an accurate map of the relative stopping power (RSP) of the patient is needed. The RSP is the stopping power of the tissue relative to the stopping power of water. When using conventional x-ray CT, one has to convert from Hounsfield units to stopping power which adds additional uncertainty. By using the same particles for imaging as used in treatment, this conversion uncertainty is avoided.

2.5.1   x-ray CT

The basis of x-ray computed tomography (CT) is the differential absorption of x-rays by various tissues. For example, bone and small calcifications absorb x-rays much more effectively than soft tissue. The basic principle behind CT, as shown in Figure 2.10, is that the two-dimensional structure of an object can be reconstructed from a series of one-dimensional projections acquired at different angles, followed by appropriate image reconstruction. A bank of solid-state detectors is situated opposite the x-ray tube, and together they record a one-dimensional projection of the patient. The x-ray source and detectors are rotated through one complete revolution around the patient, with data being acquired essentially continuously. [15]
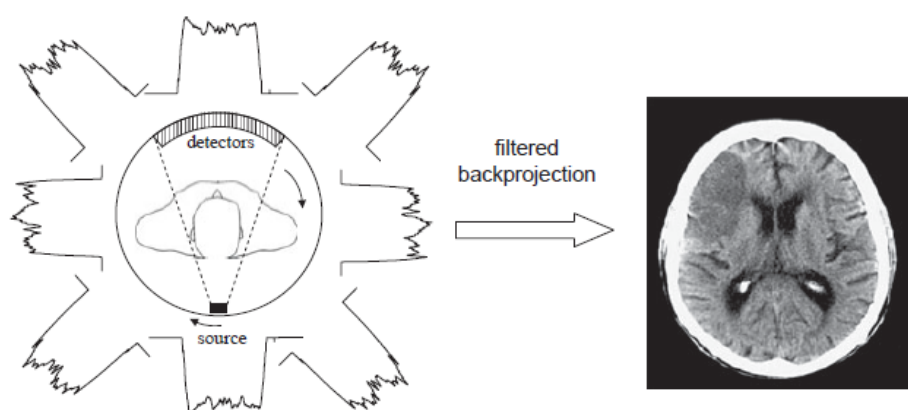
Figure 2.10: The physical principle of computed tomography involves synchronous rotation of the X-ray tube and multiple detectors to record a series of one-dimensional projections. The CT image (right) is produced by the process of filtered backprojection.[15]

Most commercial scanners use a wide x-ray fan-beam and between 512 and 768 detectors.

The beam is collimated to restrict the angular width to 45-60° and the slice thickness to 1-5 mm, typically. The scanner usually operates with an effective x-ray energy of 70-80 keV. The rotation speed is typically one per second, and the spatial resolution of the reconstructed image is typically ~ 0.35 mm. [15]

A CT image does not directly display a map of the spatially-dependent tissue attenuation coefficients but rather a map of the tissue CT numbers, which are defined as follows

$$CT_o = 1000 \frac{\mu_o - \mu_{H_2O}}{\mu_{H_2O}} \tag{2.24}$$

where CT_o is the CT number with values expressed in Hounsfield units (HU), μ_o is the linear attenuation coefficient of the tissue in each pixel and μ_{H_2O} is the linear attenuation coefficient of water. CT numbers range from -1000 for air and up to 3000 for dense bone. [15]

CT images can be used to derive RSP maps based on a predetermined linear relationship between CT numbers and RSP. The calibration curve is determined for each CT scanner used for proton treatment planning, and the accuracy of this calibration is critical to the accuracy of dose calculation. One way to determine this calibration curve is to use a stoichiometric calibration. This method determines the calibration curve based on theoretical CT numbers and RSPs of human body tissues. This method gives an uncertainty of about 3.5% in the RSP estimation. [16]

The uncertainty in the RSP estimations can be lowered by using dual energy CT (DECT). One study found that using DECT can reduce the range uncertainty to about 2.2% [17].

2.5.2   pCT

Proton computed tomography (pCT) has a large potential to reduce range uncertainties in proton therapy treatment planning. Its strength lies in the direct reconstruction of a 3D map of RSP values in the patient. [18] It has been found that pCT can further improve range accuracy compared to DECT [19].

The concept of modern pCT scanners is based on the tracking of each proton, measuring the direction and position before and after the imaged object and registering the residual energy or range after the object is crossed. Therefore, a typical pCT system must include thin tracking detectors and an energy/range detector. [18]

Due to multiple Coulomb scattering, the protons do not cross the target in a straight line. This affects the spatial resolution of pCT. Trajectory estimation methods using most likely path formalism are employed to reconstruct the trajectory of every single proton. [18]

The goal of the Bergen pCT collaboration is to design and build a pCT prototype. This prototype will not contain a front tracker but rather use information from the delivery system of the beam. This is only possible when using a pencil beam. On the rear end of the object being imaged, there will be a Digital Tracking Calorimeter (DTC) that works as both tracking and range/energy detector. [18]

The DTC will be constructed by a total of 43 detector layers. The first two layers will be tracking layers with a minimal amount of material to avoid unnecessary scattering. [18]

Chapter 3

Silicon Pixel Sensor - ALPIDE

3.1   Pixel Detectors

"Pixel", short for "picture element", is used in image processing to describe the smallest discernable element in a given process or device. A pixel detector is a device able to detect an image, and the size of the pixel corresponds to the granularity of the image. [20]

For a detector to be used in particle physics it needs to be able to study short-lived particles and cope with the high interaction rates and energies of modern particle accelerators. These requirements are met by pixel detectors with high granularity and good time and spatial resolution. [20]

In silicon pixel detectors, charge is generated in a doped silicon sensor and read out by electronics. In hybrid pixel detectors, the electronics and sensors are fabricated separately and then mated. The basic building block of a hybrid pixel detector is sketched in Figure 3.1. An ionising particle crossing the sensor generates charges that move in the depletion region under the action of an electric field and generate signals. In the electronics, the signals are amplified, and hit pixels are identified and stored. Several thousands of pixel cells can be put together in a matrix covering a few square centimetres using planar integration technology. [20]
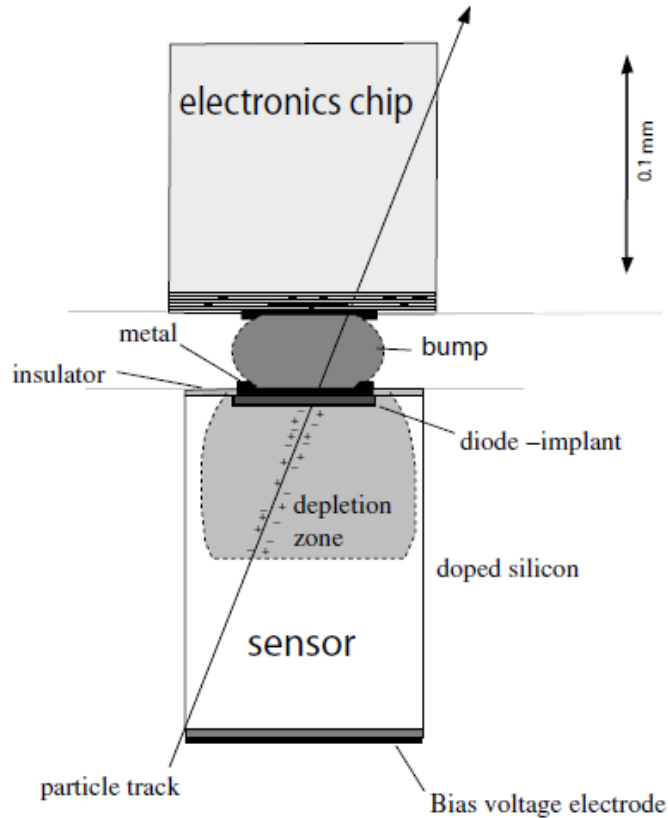
Figure 3.1: Schematic view of one pixel cell, the basic building block of a hybrid pixel detector. [20]

3.1.1 Monolithic Active Pixel Sensors (MAPS)

MAPS (Monolithic Active Pixel Sensors) are made in CMOS (Complementary Metal-Oxide-Semiconductor) technology. A pixel sensor is called monolithic when both the sensor and readout electronics are integrated into one piece of silicon. One of the advantages of monolithic sensors is that it avoids connection issues, which reduces the capacitance of each pixel and gives a very low-noise performance. [20, 21] Other advantages of MAPS detectors are low power consumption, high speed and high radiation resistance. [21]

A typical cross-section of a MAPS detector can be seen in Figure 3.2. An n-well on a p-type epitaxial layer collects the charge generated by an ionising particle. The epitaxial layer is mainly undepleted, in Figure 3.2 the depletion zone is the area between the two dashed lines. [22] The charge is primarily collected through diffusion as most of the epitaxial layer is free of the electric field. This results in a long collection time of approximately 100 ns. [23] The NMOS transistors are placed in a p-well to prevent them from acting as collection electrodes. [22]
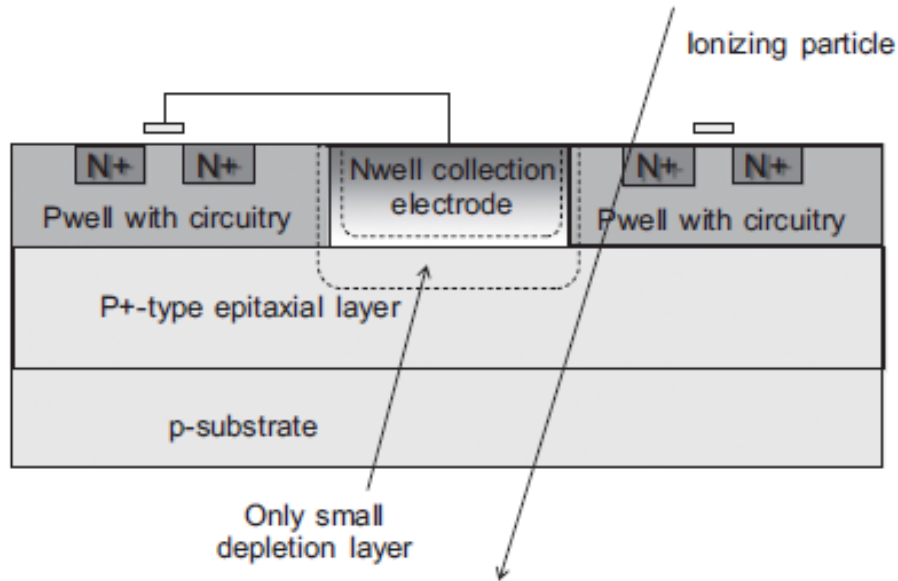
Figure 3.2: Cross section of a MAPS detector [22]

3.1.2 Clusters

A group of pixels registering a signal from the same particle is called a cluster. Charge carriers generated in the field free epitaxial layer diffuse isotropically inside the active volume of the detector. The collected charge is shared between neighbouring pixels, creating clusters. [23]

When a charged particle passes through a pixel detector between two pixels, the charge will be shared between them, and they can both register a hit. If the particle hits near a corner of a pixel, the charge is likely to be shared between four pixels. [20]

The size of the clusters can be influenced by the charge threshold of the detector. If the threshold is lowered, more neighbouring pixels can register a hit. Temperature can also affect cluster size as it affects the charge diffusion.

3.2 The ALICE Pixel Detector

The ALICE pixel detector (ALPIDE) is based on CMOS Monolithic Active Pixel Sensor (MAPS) technology. It was designed for the upgrade of the Inner Tracking System (ITS) of the ALICE (A Large Ion Collider Experiment) experiment at the CERN Large Hadron Collider (LHC). The new ITS consists of seven layers, three in the inner barrel and four in the outer barrel. Figure 3.3 shows the layout of the ITS after the upgrade. [24]
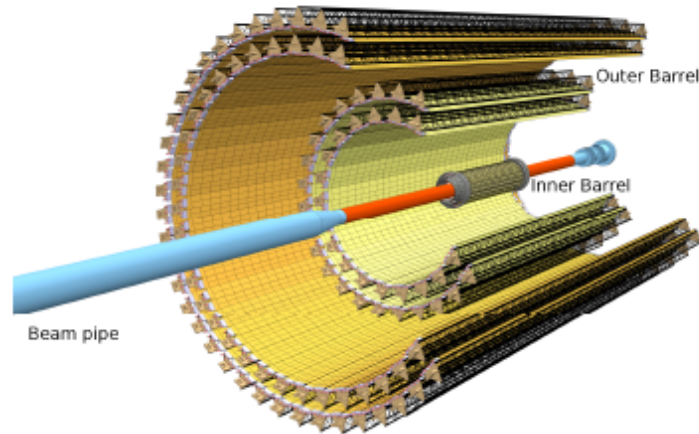
Figure 3.3: Schematic layout of the ALICE ITS after the upgrade [24]

The upgrade required a sensor with detection efficiency above 99%, fake-hit probability below 10^{-5} and a spatial resolution of 5 μm. The ALPIDE meets all these requirements. For the inner barrel a chip thickness of 50 μm was required, while the outer barrel required a chip thickness of 100 μm. [25]

3.3 ALPIDE Architecture

The ALPIDE measures 15 mm by 30 mm and contains a matrix of 512 × 1024 sensitive pixels. Each pixel measures 29.24μm by 26.88μm. Figure 3.4 shows a 3D model of 2 × 2 pixels with a total thickness of 50 μm.
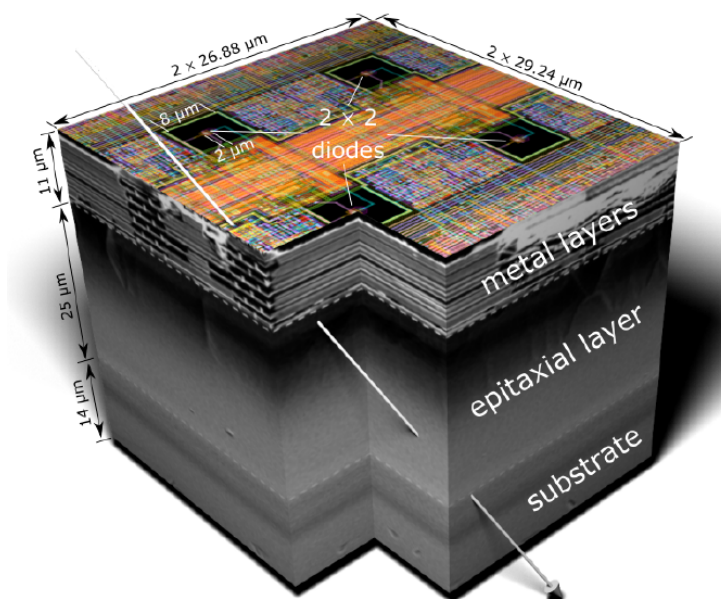
Figure 3.4: 3D model of 2 × 2 ALPIDE pixels [26]

The pixel matrix is divided into 32 readout regions, with each region containing 16 double columns. Each of the 512 double columns has a priority encoder in the middle of the double column. At the bottom of the chip, right below the last row of pixels, a periphery circuit region is located. The periphery measures 1.2 mm × 30 mm and includes readout and control functionalities. [27] Figure 3.5 shows the general architecture of the ALPIDE chip.
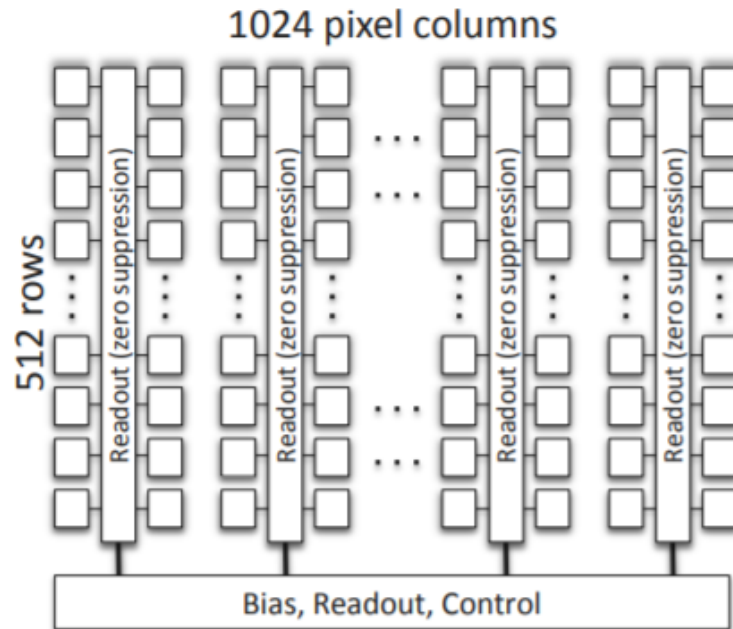
Figure 3.5: General architecture of the ALPIDE chip [27]

3.4   ALPIDE Operation

Each pixel cell contains a sensing diode, a front-end amplifying and shaping stage, a discriminator and a digital section. The front-end and the discriminator are continuously active. The front-end output has a peaking time of the order of 2 μs, while the discriminated pulse has a typical duration of 10 μs. [27] Figure 3.6 shows the block diagram for the pixel cell.
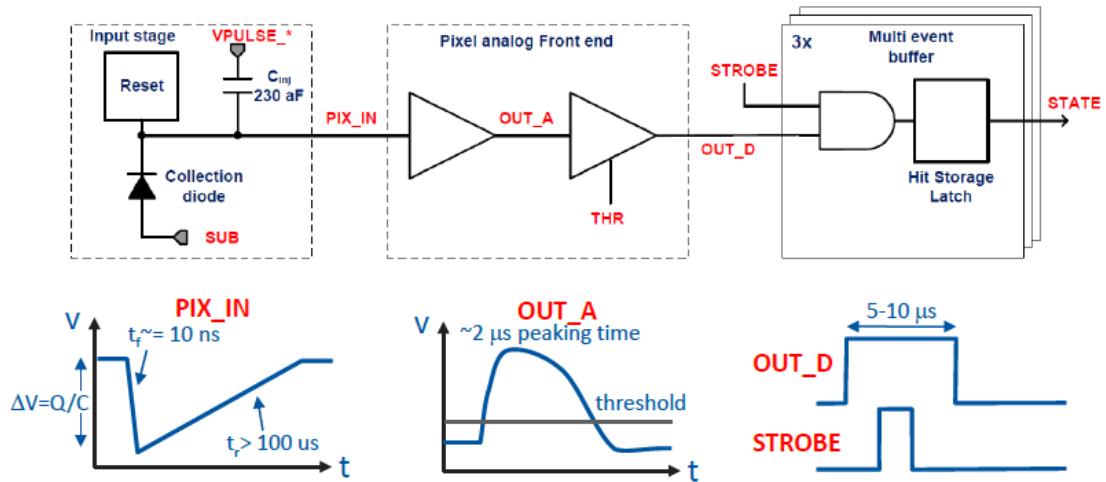
Figure 3.6: Block diagram of the pixel cell [27]

A common threshold level is applied to all the pixels. The global STROBE signals control the latching of the discriminated hits in the storage registers. A pixel hit is latched into one of the three in-pixel memory cells if a STROBE pulse is applied to the selected cell while the front-end output is above the threshold. Three distinct STROBE signals are generated at the periphery and globally applied to all pixels, controlling the storage of the pixel hit information in the pixel event buffers. [27]

Each pixel contains a Mask and a Pulse Enable register. The Mask register can be used to force low the digital output of the pixel. A masked pixel is skipped by the readout and does not appear in event frames. The Pulse Enable registers are used to enable test pulsing functionalities. A hit can be forced through analog pulsing by using a test charge injection capacitor or through digital pulsing by directly setting the pixel state register. [27]

3.4.1 Analog Front-End

A detailed scheme of the pixel front-end circuit can be seen in Figure 3.7.
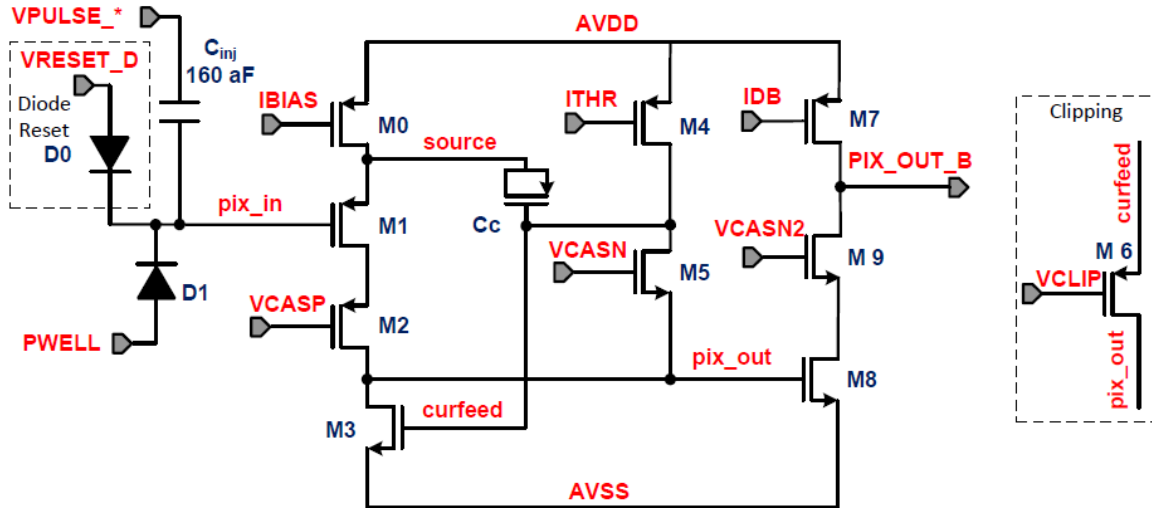
Figure 3.7: Front-end scheme of the ALPIDE [27]

The D1 diode is the sensor p-n junction. The input node is continuously reset by the D0 diode. VRESET_D controls the reset voltage of the charge collecting node pix_in. An electrical test charge can be injected by applying a voltage pulse of controllable amplitude to the VPULSE pin of the C_{inj} capacitor. A particle hit will lower the potential at the pixel input pix_in by a few tens of mV. This causes the potential on the output node pix_out to swing upwards by several hundreds of mV. If the charge deposit from the particle hit is sufficiently large to overcome the threshold, PIX_OUT_B is driven to zero. The active low PIX_OUT_B signal is applied to the digital section of the pixel, where it is used to set the hit status register. [27]

The charge threshold of the pixel is set by ITHR, IDB, and VCASN. Increasing ITHR or IDB increases the charge threshold. The threshold is decreased when increasing VCASN. [27]

3.4.2 Triggering and Framing

A frame is a collection of pixel states at a particular time. When a trigger is received, a frame is generated and transmitted off-chip. Each pixel on the ALPIDE has a Multi Event Buffer (MEB). The MEB is a set of three in-pixel data storage elements called buffers. This enables the storage of three full frames without the completion of a matrix readout or any data loss. [27]

The writing and reading of the pixels is based on the management of the pixel MEBs, this is implemented in the Framing and Management Unit (FROMU). The management scheme for the pixel MEBs is illustrated in Figure 3.8. [27]
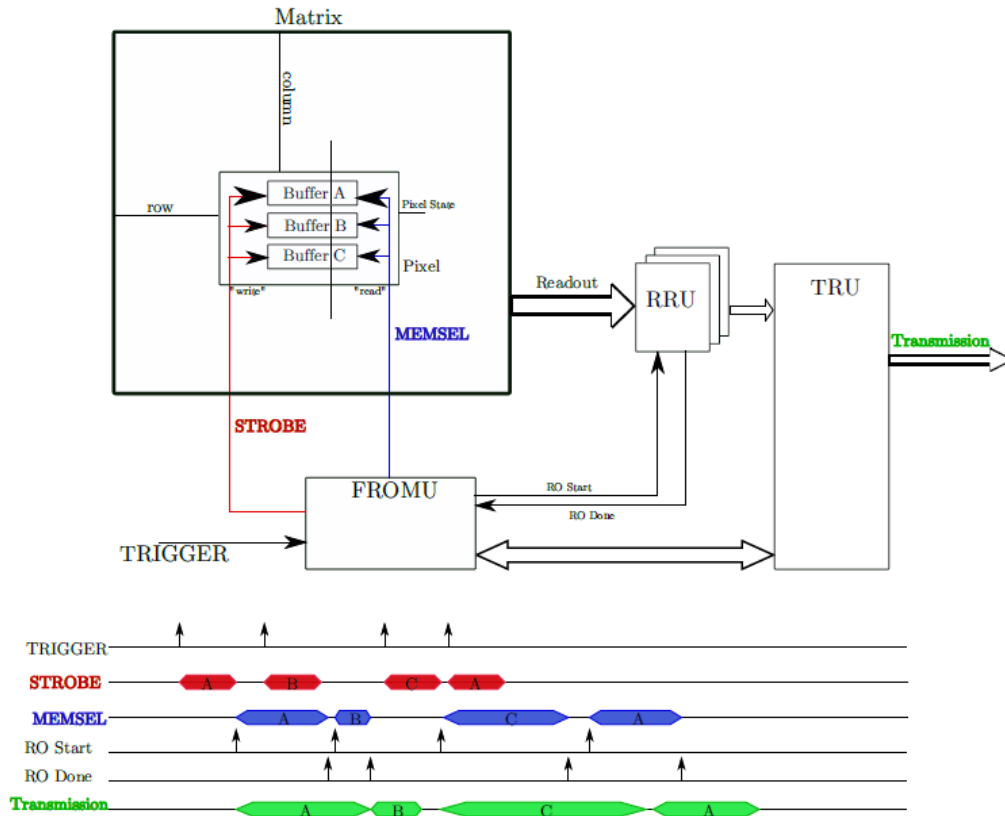
Figure 3.8: Pixel MEB management scheme [27]

There are three distinct STROBE signals, one for each buffer. When a trigger is received from an external source, the timed assertions of one of the three global STROBE signals are initiated. This timed STROBE assertion is called framing interval or window. It can also be initiated by an internal sequencer. The strobe signal is distributed to all pixels from the periphery and controls the recording of the pixel discriminator outputs in the storage register. The connection between the output of the pixel and the inputs of the priority encoder is governed by the three global MEMSEL signals. [27]

When a STROBE assertion is finished, the readout of the pixel buffer starts. Each of the 32 matrix regions has a corresponding region readout unit (RRU). All 32 regions are read out simultaneously by their respective RRUs. The RRUs store the data in local memories before the top readout unit (TRU) fetches the information and transmits it off-chip. [27]

Two MEB management schemes, called readout modes, are supported: Triggered and Continuous.

In triggered mode, the framing intervals are typically initiated by a trigger from an external source. The triggered mode is intended to use relatively short framing intervals. In this mode, the chip prioritises events already stored in the matrix over new incoming triggers. If a trigger is received while all three buffers are full, it will not generate a new framing interval. [27]

In continuous mode, the framing intervals are typically initiated by an internal sequencer. The framing intervals are usually longer than those in triggered mode. The time between framing intervals is maintained as low as possible. In continuous mode, new frame requests are prioritised over data already stored in the matrix. The ALPIDE ensures that at least one buffer is always available. If the last free buffer receives a framing request, the chip will interrupt the current frame readout to free up one of the buffers. [27]

3.4.3   Data Format

Table 3.1 lists the valid data words and their functionalities.

Data Word	Length [bits]	Function
IDLE	8	Used as a filler whenever data is not ready to be transmitted
CHIP HEADER	16	Data word transmitted at the beginning of each data packet
CHIP TRAILER	8	Data word transmitted at the end of each data frame
CHIP EMPTY FRAME	16	Used when a fully readout event is actually completely empty
REGION HEADER	8	Used to indicate the beginning of transmission of data for a particular region
DATA SHORT	16	Data word containing the geographical location of a single pixel
DATA LONG	24	Data word used to enable the compression of up to 8 pixels via a bit map
BUSY ON	8	Code word transmitted on assertion of the BUSY status
BUSY OFF	8	Code word transmitted on the serial port on de-assertion of the BUSY status

Table 3.1: Data Format adopted in ALPIDE chip [27]

3.5   Threshold Scans

To find the threshold of an ALPIDE chip, a threshold scan is conducted on a subset of the pixels. The threshold of a pixel is the amount of charge needed for the pixel to register a hit 50% of the time.

In a threshold scan, the in-pixel analog pulsing is used to inject a charge, q_{inj}, into the pixel. Starting at a low charge value, each pixel is injected N_{inj} times per charge. The charge is increased in increments of 1 DAC up to a set charge value. For each charge, the number of hits in each pixel is registered.

When plotting the number of hits per charge value for a single pixel, one can see a curve that starts at 0 and increases rapidly when approaching the threshold value of the pixel and then stabilises at the number of triggers per charge. The threshold is defined as the charge value where the pixel triggers 50% of the time. This threshold can be found by fitting the data points with the following error function:

$$f(x) = \frac{1}{2}\left[1 + erf\left(\frac{x-\mu}{\sqrt{2}\sigma}\right)\right] \tag{3.1}$$

where x is the injected charge, μ is the threshold value, and σ is the temporal noise of the pixel. This fitted cure is often referred to as an S-curve. By fitting an S-curve to every scanned pixel, one can find the threshold distribution of the chip. The mean of this distribution is the threshold value for the chip.

3.6 The Bergen pCT

3.6.1 Detector Design

The Bergen pCT prototype will use a 43 layer Digital Tracking Calorimeter (DTC) with ALPIDE sensors. Figure 3.9 shows the general design of the prototype. The first two layers in the DTC are thin tracking layers, followed by 41 detector/absorber sandwich layers (calorimeter). Each layer will have a sensitive area of about 27 cm × 16.6 cm. [18]
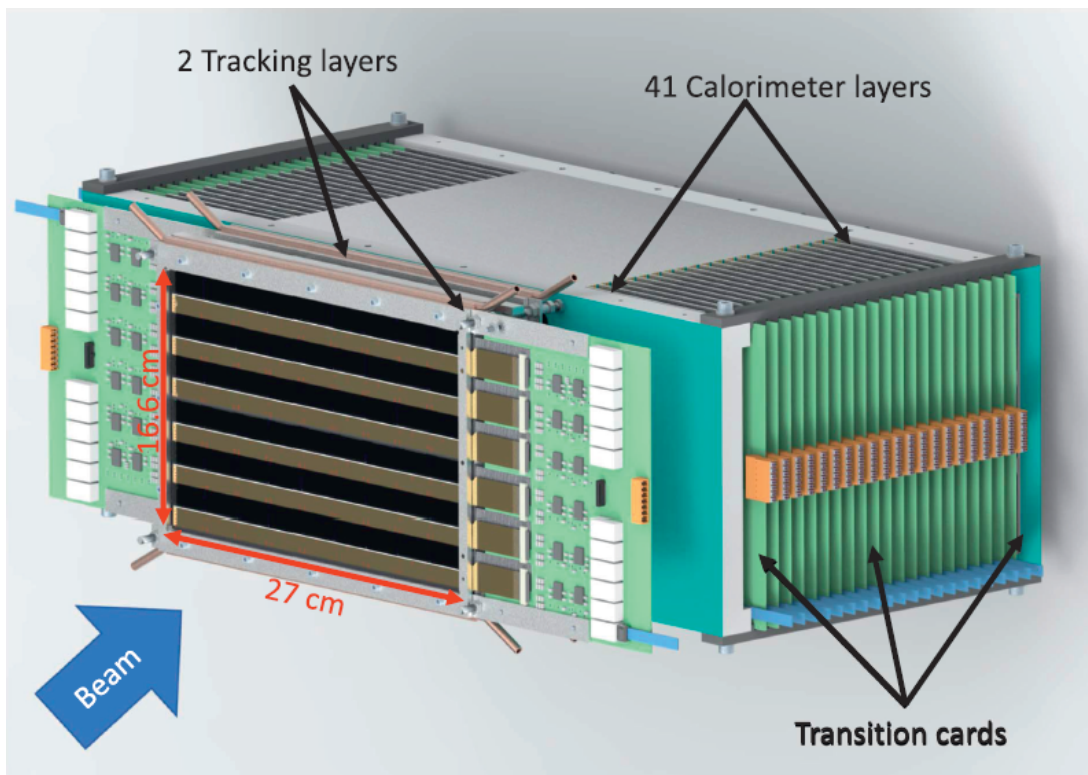

Figure 3.9: General structure of the Bergen pCT system. [18]

The general structure and design of a layer is the same for both tracking and calorimeter layers. For the calorimeter layers three strings, each consisting of nine 100 μm ALPIDE chips

mounted on flex cable, are glued to an aluminium carrier of dimension 100 mm × 290 mm × 1 mm called a slab. One top slab and one bottom slab make up one half layer as seen in Figure 3.10. In a half layer, almost half of the area is not covered by the ALPIDE chips, therefor another half layer is positioned so that the sensitive areas of one half layer cover the non-sensitive areas of the other. Each full layer then contains 108 ALPIDE chips. [18]

For the calorimeter layers, a 1.5 mm aluminium plate will be used in addition to the 1 mm thick aluminium carrier plates of the slabs giving a total absorber thickness of 3.5 mm. This gives each layer a water equivalent thickness of 7.5 mm. Figure 3.11 shows a schematic of the layer structure. With its 41 calorimeter layers, the DTC is able to fully contain the range of a 230 MeV proton beam. [18]
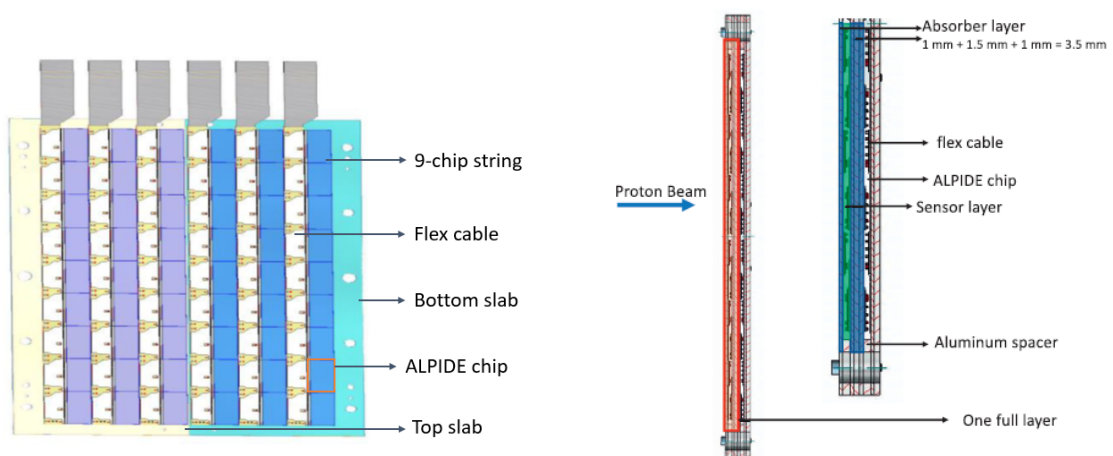
Figure 3.10: Half layer consisting of a top slab and a bottom slab [18]

Figure 3.11: Schematic side view of two DTC layers (left) and a half layer with details (right) [18]

To minimise the material in the tracking layers, 50 μm ALPIDE chips will be mounted on ~ 0.2 mm thick carbon-epoxy sandwich sheets of area 200 mm × 290 mm. Two half layers will be placed facing each other with a 2 mm air gap ensured by aluminium spacers.

3.6.2   Readout and DAQ

The pCT data acquisition (DAQ) and run-control system are built up by three parts: the frontend electronics, the transition card, and the pCT readout unit (pRU). A schematic of the Bergen pCT system electronics architecture is shown in Figure 3.12. The frontend electronics and transition cards are placed in the high radiation zone. To reduce radiation damage the pRU is placed at least 2 m from the detector centre. [18]
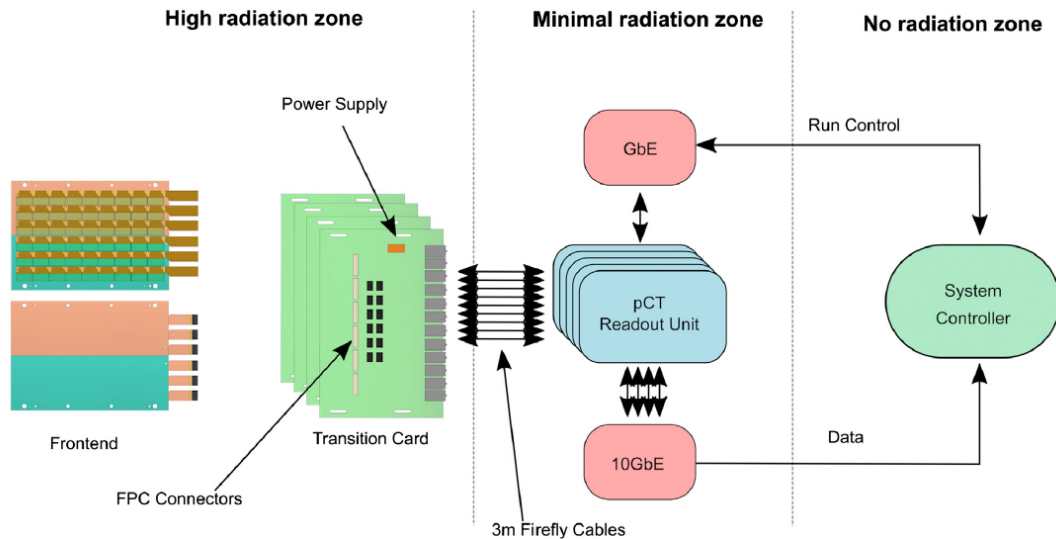
Figure 3.12: Electronics architecture for the pCT system. [18]

The transition card is used as an intermediate medium between the frontend and readout electronics for each layer. It also delivers stable power to the sensors. [18]

The pCT Readout Unit (pRU) is under development but is clearly defined based on testing with the Xilinx VCU118 Evaluation Kit [18].

The data format, of which data is offloaded from the pRU, contains four types of pRU words:

- DATA_WORD

- TAG_HEADER_WORD

- TAG_TRAILER_WORD

- TAG_EMPTY_WORD

Each word consists of 128 bits. A total of 16 bits are occupied by identifiers for word type, readout unit, stave and chip. This leaves 112 bits available for other content.

For a DATA_WORD, the 112 available bits are used for collection of ALPIDE data. Redundant ALPIDE data words are filtered by default.

A TAG_HEADER_WORD is transmitted before any ALPDE data to provide information about time and space for frame reconstruction. It is followed by one or more DATA_WORD, and finally, a TAG_TRAILER_WORD is transmitted to indicate that a whole ALPIDE frame has been read out. The TAG_TRAILER_WORD holds information regarding frame size and any errors observed during transmission.

A TAG_EMPTY_WORD is transmitted whenever an ALPIDE contains no pixel hits. The tag is not accompanied by a header or trailer tag and is invented to minimise the number of bits transmitted. [28]

Chapter 4

Optimisation of ALPIDE's Configuration Parameters

This chapter introduces threshold measurements of the ALPIDE and investigates the effect of some analog front-end settings on the threshold. The effect of the analog front-end settings and strobe length on noise is also investigated and data rates in pedestal runs are calculated to see the effect of masking noisy pixels. Finally, it looks at how the threshold influences measurements with an Am-241 source. This is important for the final pCT system as the cluster size can be used as a measure of the deposited energy.

4.1 Setups

4.1.1 8-ALPIDE setup

This setup contained 8 ALPIDE chips distributed over 4 layers. Figure 4.1 shows a schematic view of the readout. Two ALPIDEs were mounted on a flexcable situated in a Yamaichi frame. A transition card was used as an intermediate between the readout unit (VCU118) and the ALPIDE chips. Each ALPIDE module was connected to the transition card via ZIF-connectors, and communication between the transition card and the readout unit was via a samtec firefly cable.
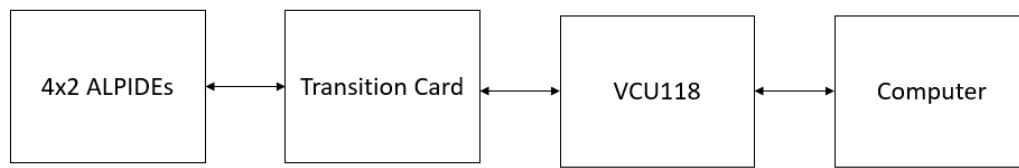
Figure 4.1: Schematic view of readout system with 8 ALPIDE chips

Due to an issue with chip ID 7, only chips 0-6 are used in the analysis.

4.1.2   Single ALPIDE

A single ALPIDE chip was connected to a Data Acquisition (DAQ) board. The DAQ board was powered with 5 V provided by a power supply. A signal generator was used as an external trigger source. The DAQ board was connected to a computer through a micro USB cable. Figure 4.2 shows the schematics of the experimental setup. Both the power supply and the signal generator could be controlled from the computer using python scripts. These scripts were used to set the wanted settings for the signal generator and power supply. The signal generator delivered the triggers in trains of 100 triggers each. There was a 100 ms pause between each train for the DAQ board to offload the information.
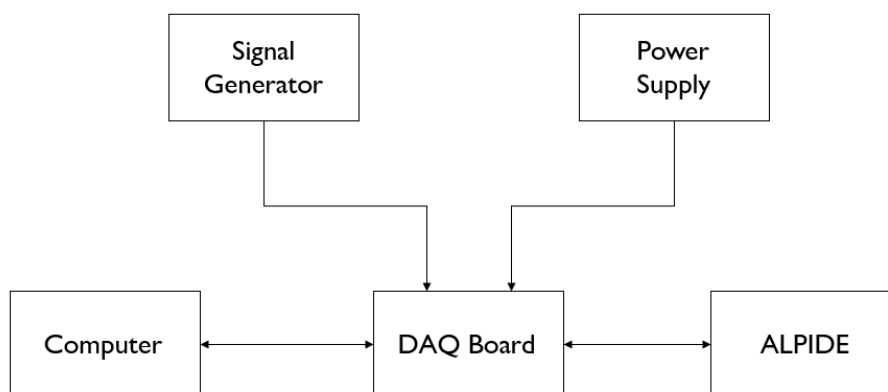
Figure 4.2: Experimental setup

Two separate ALPIDE chips were used in this setup, hereafter referred to as Chip 1 and Chip 2.

4.1.3 Electromagnetic Calorimeter with ALPIDE

The setup used an Electromagnetic Pixel Calorimeter prototype called EPICAL-2. This prototype consists of 24 layers, each containing two ALPIDE-chips with chip and flex cables and a 3 mm tungsten absorber. Figure 4.3 shows the design drawing of the prototype. The sensitive area is 3 cm × 3 cm. Each layer has a total thickness of 3.5 mm. The stack of 24 layers is mounted in an aluminium casing with water cooling. [29]
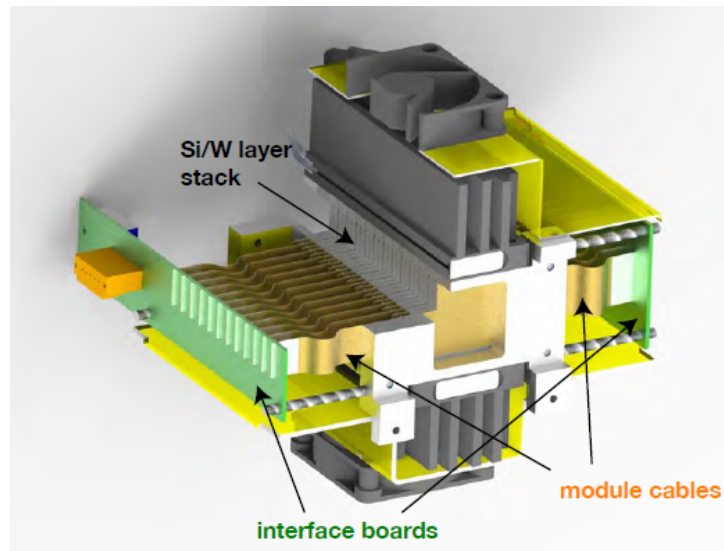
Figure 4.3: Design drawing of the EPICAL-2 prototype. [29]

Figure 4.4 shows a schematic view of the readout system of the EPICAL-2 detector. 12 layer cables extend from both sides of the detector and connect to an interface board using ZIF connectors. [29]

Figure 4.4: Schematic view of the readout system of the EPICAL-2 detector. [29]

Trigger signals were initialised by two scintillation tiles placed in front of the EPICAL-2. A trigger was delivered when an electron passed through the scintillation tiles. The tiles had

a thickness of 3 mm and an area of 30×30 mm^2 and were read out by a low noise silicon photo-multiplier mounted on a printed circuit board. The tiles were coated with a reflective adhesive foil and covered with black light-tight tape to increase the light yield. [29]

4.2   Threshold vs Analog Front-End Settings

For a functional pCT system using ALPIDE chips, it will be necessary for all of the chips in the system to have approximately the same threshold. This is important to get the same response from all of the chips under the same conditions. Therefore, it is of interest to investigate how a chips threshold is affected by the analog front-end settings and whether or not this response looks the same for different chips. The data analysed in this section was acquired using the setup described in section 4.1.1.

In this section, a threshold scan was run by injecting all pixels one time per charge starting at $q_{inj} = 0$ DAC and ending with $q_{inj} = 50$ DAC. The threshold for each pixel was found by taking the end charge and subtracting the number of registered hits in the pixel. The threshold of the chip as a whole was defined as the mean value of the pixel thresholds.

The default values for the front-end settings are: VCASN = 50 DAC, ITHR = 50 DAC and IDB = 29 DAC. The DAC unit is an arbitrary unit used for the ALPIDE.

To decide what range of values for each front-end setting would give usable results, tests were performed on chip 1. Only one setting was adjusted at one time, the other settings were kept at their default. For VCASN values at 40 or lower, the threshold exceeded 50 and was not measurable with the current setup. When the VCASN value was higher than 55, the measured threshold was very low (<1 DAC). It was also found that the threshold changed rapidly around the default setting, and it would be useful to have measurements with small changes in VCASN values around this area. The ITHR values gave reasonable threshold measurements when using values between 30 and 70. For the IDB measurements, values from 1 to 70 were used. Changing the IDB value gave a much smaller response in threshold value than the other two settings. It also appeared to need higher statistics as the curve was quite jagged. The resulting curves for chip 1 can be seen in Figure 4.5
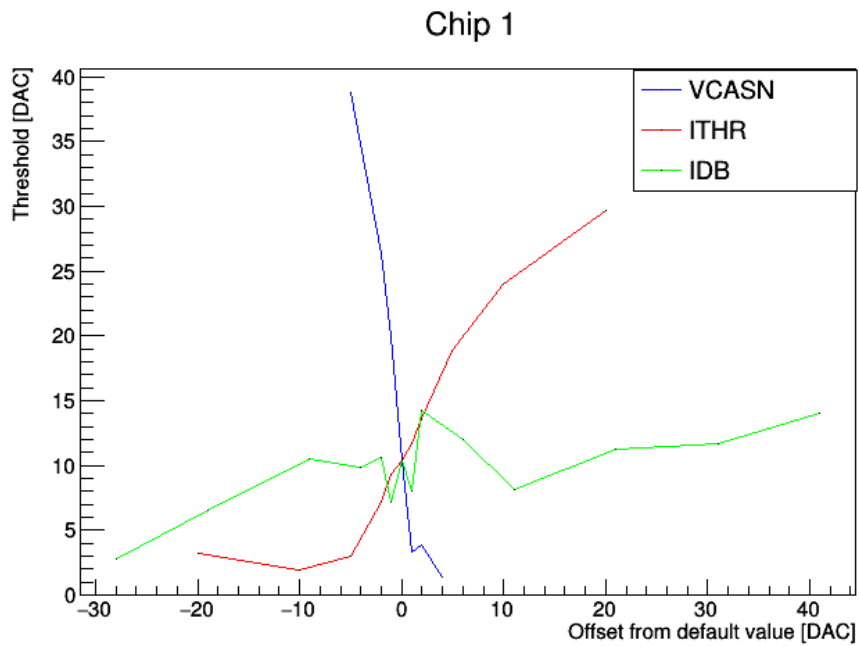
Figure 4.5: Curves showing threshold values for changing front-end settings for chip 1

Based on the measurements performed on chip 1 it was decided to only make measurements for varying VCASN and ITHR values for the remaining chips. VCASN values were set from 45 to 54 and ITHR values from 30 to 70. All of the functioning chips (0-6) were tested with the same values for VCASN and ITHR.

4.2.1 Results

With increasing ITHR values the threshold increases. From Figure 4.6 one can see that there is a large variation in the curves for each chip. At an offset of -20, most of the curves approach zero. With increasing values of ITHR, the spread in threshold values for the different chips increase.
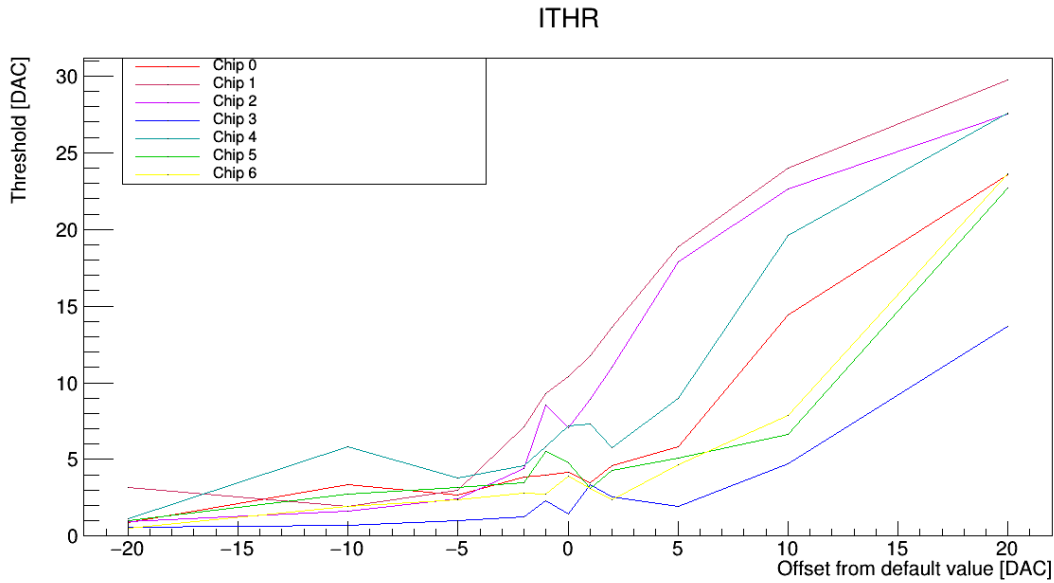
Figure 4.6: Threshold dependency of ITHR value for different chips

Figure 4.7 shows the threshold curves for varying VCASN values. Here the threshold increases with decreasing values of VCASN. The increase of threshold with decreasing VCASN values is much steeper than that for increasing ITHR values. When increasing the VCASN value from the default, the curve flattens at low threshold values.
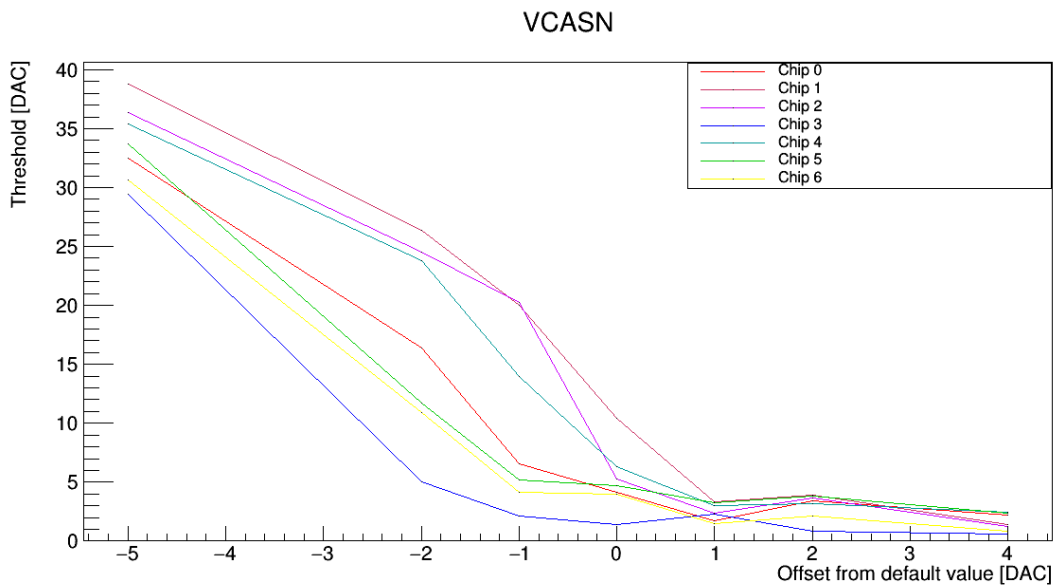
Figure 4.7: Threshold dependency of VCASN value for different chips

Although the general effect of changing ITHR or VCASN is the same for all chips, there is a large spread between the individual curves. Both ITHR and VCASN can be adjusted to increase the charge threshold of a chip. Even a small decrease in VCANS gives a significant increase in the threshold. Increasing the ITHR value also increases the charge threshold, but

the increase is not as significant as for VCASN. Therefore, when adjusting the threshold of chips, it is useful to adjust VCASN if the threshold is far from the wanted threshold value while changing ITHR is more suitable for fine-tuning.

4.3 Noise Studies

The measurements used in this section were obtained using the setups described in section 4.1.1 and 4.1.3.

4.3.1 Analog Front-End

The charge threshold of the chip affects the noise level. Whenever the threshold is lowered, the chip gets more susceptible to noise. To see the effect of this, measurements were made with different settings for ITHR and VCASN. All chips were triggered 100k times per setting. The trigger delay was set to 10 μs with a 9.75 μs strobe length. No pixels were masked during the data acquisition.

The ITHR setting was varied between 20 and 70 DAC while keeping VCASN constant at 50 DAC. For each setting, the number of registered hits was found, and the fake-hit rate (FHR) was calculated as follows

$$\text{FHR} = \frac{\# \text{ hits}}{\# \text{ pixels} \times \# \text{ events}} \tag{4.1}$$

The fake-hit rates for varying ITHR values can be seen in Figure 4.8.
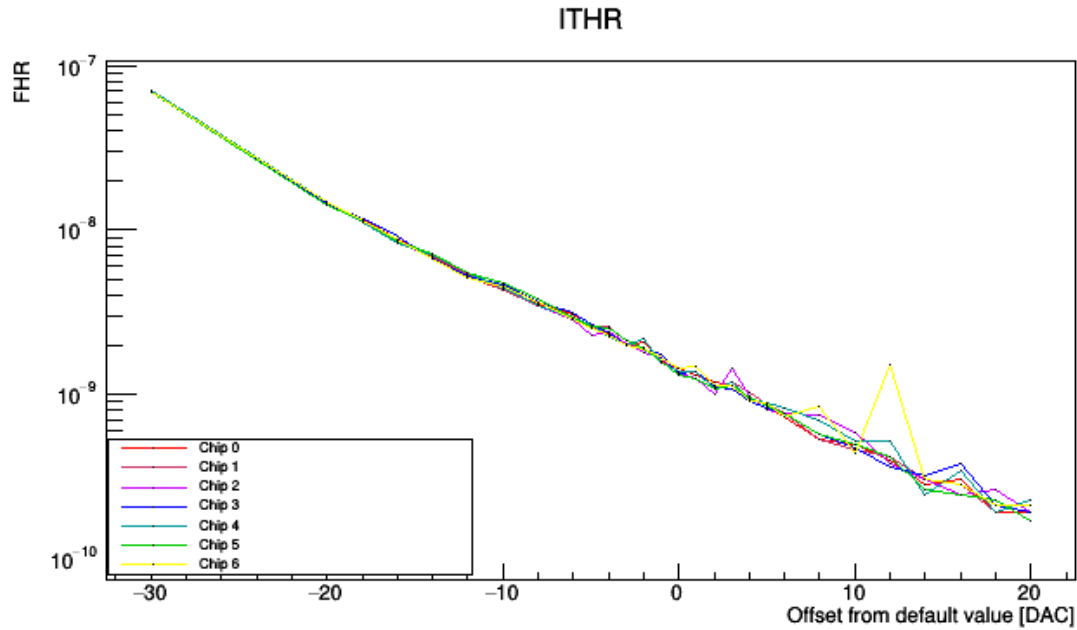
Figure 4.8: Fake-hit rates for varying ITHR values for chips 0-6

With varying ITHR values, the different chips have a relatively uniform response. As expected, due to the increasing threshold, the number of hits decreases with increasing ITHR values. This decrease is approximately exponential. Fitting the data with an exponential curve, e^{a+bx}, gave constant $a \approx -20.08$ and slope $b \approx -0.12$.

The VCASN settings were then varied between 30 and 64 DAC while keeping ITHR constant at 50 DAC. The fake-hit rates for varying VCASN are shown in Figure 4.9.
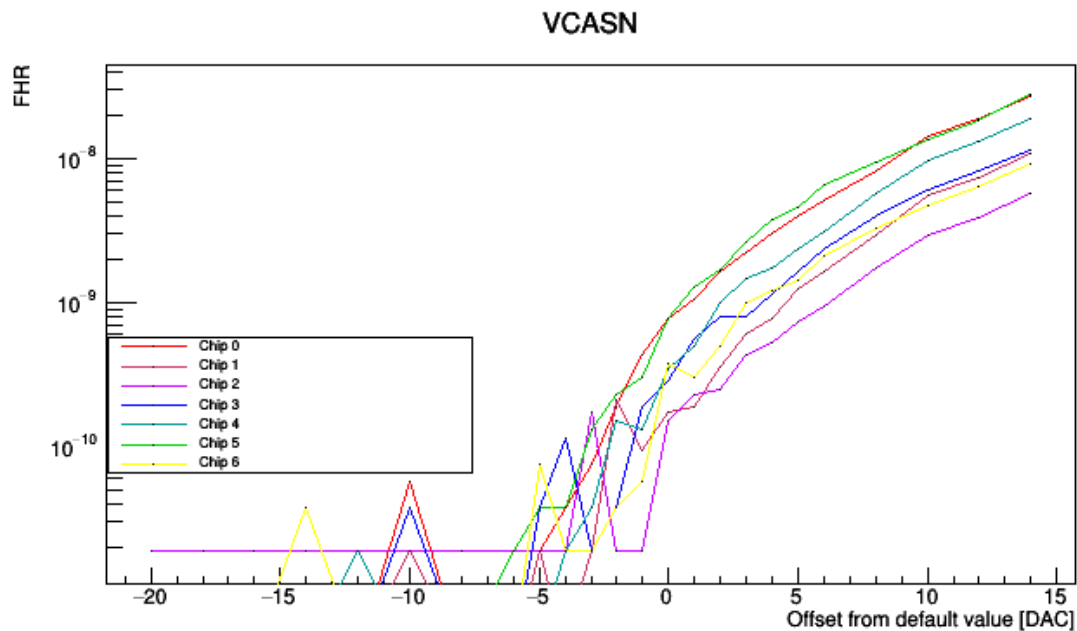

Figure 4.9: Fake-hit rates for varying VCASN values for different chips

For varying VCASN values, the curves for the different chips have a much larger spread than for varying ITHR. The number of hits quickly goes to zero when the VCASN value is decreased from the default value. This is expected as the threshold rapidly increases with decreasing VCASN.

The results show that the fake-hit rate is highly dependant on the charge threshold. At very high thresholds, the fake-hit rate drops below 10^{-10} as seen for low VCASN values. At very low thresholds, the fake-hit rate is significantly higher. The highest measured FHR value is just below 10^{-7} for ITHR = 20 DAC.

4.3.2 Strobe Length

Multiple measurements were made to investigate the effect of strobe length on the fake-hit rate. With a trigger delay of 35 μs, the strobe length was varied between 250 ns and 30 μs. The ALPIDE chips were triggered 100k times per strobe length setting. The percentage of triggers that recorded any noise was plotted as a function of strobe length. The data points appeared to be quite linear, so a linear fit was added to the plot. The final plot can be seen in Figure 4.10. The slope of the fitted line was found to be 1.10 ± 0.02.

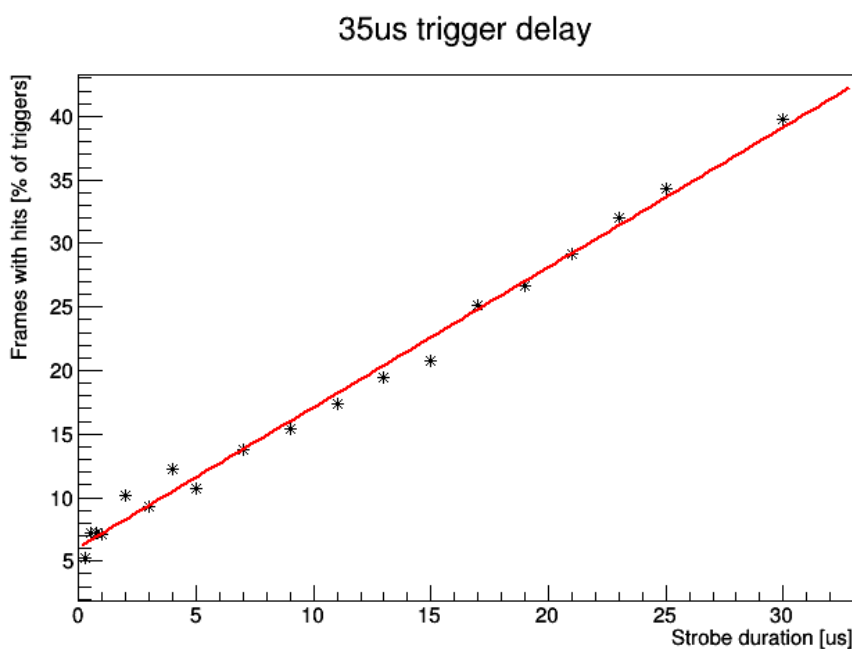Figure 4.10: % of frames containing hits as a function of strobe length. Data points are visualised as black stars. The red line shows linear fit.

This linear relationship between strobe length and registered noise substantiates the assumption that the noise is random and comes and goes, thus longer time intervals give higher chance of recording noise. The final pCT system plans to use a strobe length of 10

μs. Based on these measurements, noise will be registered for approximately 15% of all triggers when there is no radiation source.

4.3.3 Pedestal Noise

In this section, data from pedestal runs with the EPICAL-2 prototype described in section 4.1.3 is analysed. In a pedestal run the detector is not irradiated by an ionising source. Data from five different pedestal runs with the same settings will be used to get higher statistics. The run numbers and settings can be seen in Table 4.1.

Run Number	Water Temperature [°C]	Strobe Length [μs]	Recorded Events
1332	20	2	96000
1340	20	2	92000
1374	20	2	92000
1395	20	2	92000
1421	20	2	92000

Table 4.1: Pedestal run settings

The number of hits in a run was found for all pixels in the calorimeter. The results can be seen in Figure 4.11. It appears that approximately 20% of the pixels register no hits. There is a sharp drop-off to the fraction of pixels that only registered one hit.
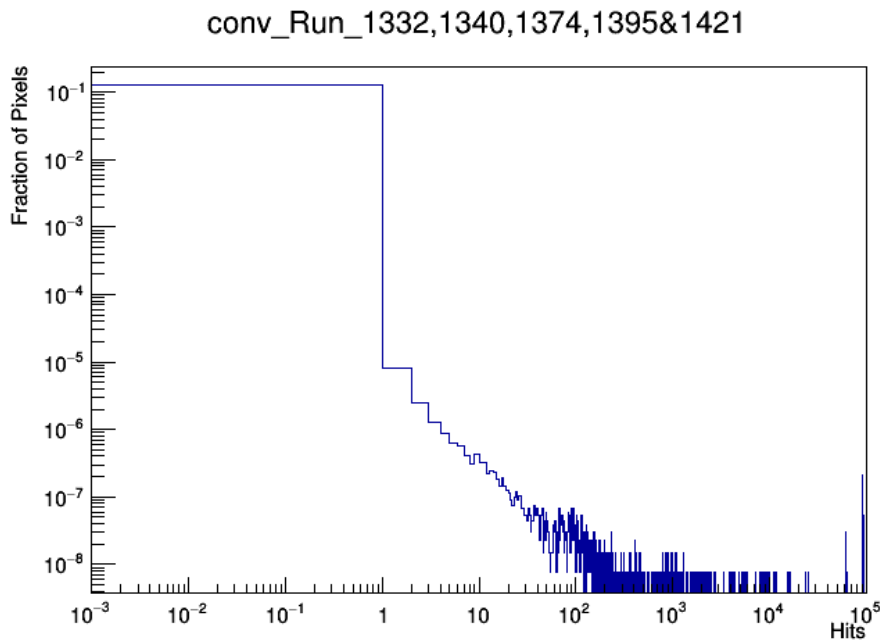

Figure 4.11: Hits per pixel for all pixels.

Only pixels with at least one hit during a run are considered in the following. The number of registered hits was found as a percentage of the total number of events for the given run for each pixel. This plot can be seen in Figure 4.12. From this plot it appears that the vast majority of pixels register hits for less than 1% of all triggers. Very few pixels register hits for more than 10% of triggers.
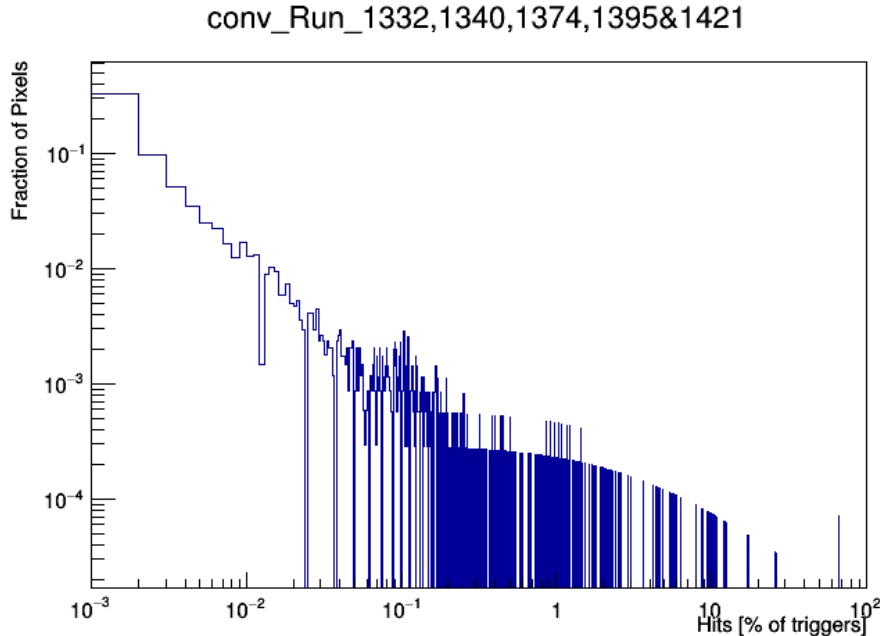

Figure 4.12: Hits per pixel for pixels with hits.

It can be assumed that pixels with a low percentage of hits only experience statistical noise that cannot be avoided. Pixels with much more hits than the expected statistical noise can be masked in data taking to reduce the amount of raw data. As seen in the previous plots, a small fraction of the pixels generate a large number of hits and may be considered for masking. In the following, calculations are performed to see how much raw data can be reduced by masking all pixels that register hits in more than a given percent of triggers.

The calculations are based on the pRU data format. To simplify the calculations, it is assumed that each registered hit generates a DATA SHORT. It is also assumed that each hit generates a REGION HEADER, with a maximum of 32 REGION HEADERs per chip per event. To find the amount of data produced per chip, the total data amount is divided by the number of chips in the EPICAL that register noise in the pedestal run. The calculated data rates listed in Table 4.2 are based on a trigger rate of 100 kHz. Data rates are calculated for a single chip, for a layer i the pCT system (108 chips) and for the total pCT system of 43 layers.

Masking Threshold [%]	Mbit/s per Chip	Mbit/s per layer	Gbit/s for total pCT system
No masking	5.89	636.2	27.4
90	2.11	227.4	9.77
50	1.58	170.3	7.32
10	1.05	113.4	4.87
1	0.28	30.0	1.29
0.1	0.053	5.78	0.25

Table 4.2: Data rates per chip, layer and total pCT system for different masking thresholds based on data from Run_1332

From the numbers in Table 4.2 it appears that masking pixels that fire for more than 90% of triggers is highly beneficial to reduce data. In the 47 chips in the EPICAL-2 this would involve masking 7 pixels in total. When lowering the masking limit to 50% one more pixel is masked and the amount of data is slightly reduced. At a 10% masking limit, 12 pixels are masked. 38 pixels are masked when the masking limit is set to 1%. If the masking limit is lowered to 0.1%, 120 pixels are masked.

4.4   Studies with Am-241 Source

To see the impact of threshold on cluster sizes, the ALPIDE chip was irradiated using an Am-241 source. The experimental setup is described in section 4.1.2. The source was an ORTEC AM-1U source with an initial activity of 370 kBq in 1975. Am-241 decays through gamma and alpha decay with a decay scheme as shown in Figure 4.13.
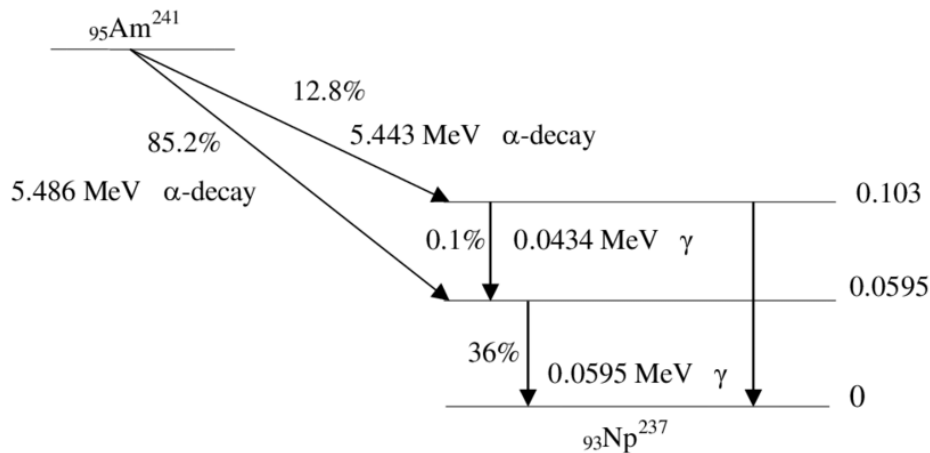

Figure 4.13: Radioactive decay scheme of Am-241 [30]

The source was placed on an aluminium stand a few cm above the chip. With an energy

of approximately 5.5 MeV, the alpha particles have a range of almost 4.2 cm in air [31]. Alpha particles hitting the ALPIDE will deposit energy that will diffuse to neighbouring pixels creating clusters. The 60 keV gammas make smaller clusters as they deposit less charge.

4.4.1 Method

The threshold was adjusted by changing the ITHR and VCASN values of the chip, all other front-end analog settings were kept at default values. In this section, the threshold was found by running a threshold scan on 1/8 of the pixels. Each pixel was injected 10 times per charge value. The strobe length was set to 9.75 μs. A S-curve was fitted for each of the tested pixels. The threshold of the chip is then found by taking the average of the threshold values from the S-curve fittings.

The measured average thresholds and their standard deviations are listed in Table 4.3. Chip 1 was tested with 12 different settings for VCASN and ITHR. For Chip 2 only 5 different settings were tested.

		Chip1		Chip 2	
ITHR	VCASN	Avg. Thr	Stdev. Thr	Avg. Thr	Stdev. Thr
30	50	8.0	0.2	12.0	0.5
50	50	11.6	0.1	20.0	0.7
55	50	14.9	0.5	-	-
60	50	16.3	0.5	23.6	0.8
70	50	18.8	0.4	-	-
75	50	19.5	0.3	-	-
80	50	21.2	0.3	30.8	0.9
90	50	23.5	0.3	-	-
50	45	25.8	0.5	39.5	1.0
50	43	36.0	0.8	-	-
50	42	41.1	0.9	-	-
50	40	54.2	2.8	-	-

Table 4.3: Measured average charge threshold and standard deviation for varying values of ITHR and VCASN.

For each setting, the ALPIDE was triggered one million times with a trigger delay of 50 μs and strobe length 49.75 μs. The hits were written to an ascii file with x-position, y-position, and event ID for each pixel hit. A script was written to identify clusters and find the size of each cluster.

Two subsequent hits were identified as part of the same cluster if they had the same event ID, the difference in the x-position was less than 4, and the difference in y-position was less than 6. The size of each cluster was entered into a 1D histogram giving a cluster size distribution as seen in Figure 4.15.

It was found that the cluster size distributions for all threshold values had a peak in cluster size equal to 1. These single-pixel hits can come from noise in the chip as well as the 60 keV gammas emitted from the Am-241 source. In Figure 4.15 single-pixel hits from pixels that registered more than 100 hits are not included. The distributions also had a Gaussian-shaped curve starting at about 10 pixels in cluster size. It is safe to assume that these large clusters are purely made from alphas. This was confirmed by shielding the source with a single piece of paper, thus stopping the alpha particles and only transmitting 60 keV gammas. When the alpha particles are stopped, only smaller clusters are made as seen in Figure 4.14.
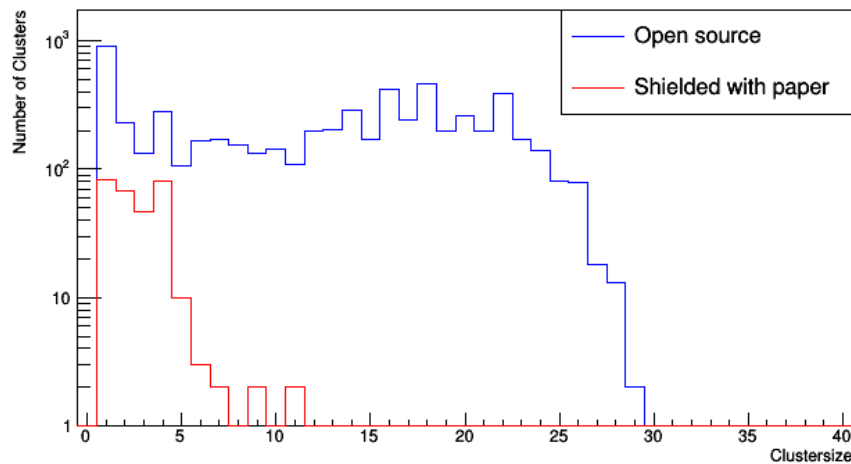

Figure 4.14: Cluster size distributions for Chip 2 at default setting with and without shielding.

As the Gaussian shape could be seen in all distributions, each distribution was fitted with a Gaussian curve, with the fitting starting at cluster size 10 pixels. Two examples of these distributions with fitted Gaussian curves can be seen in Figure 4.15.
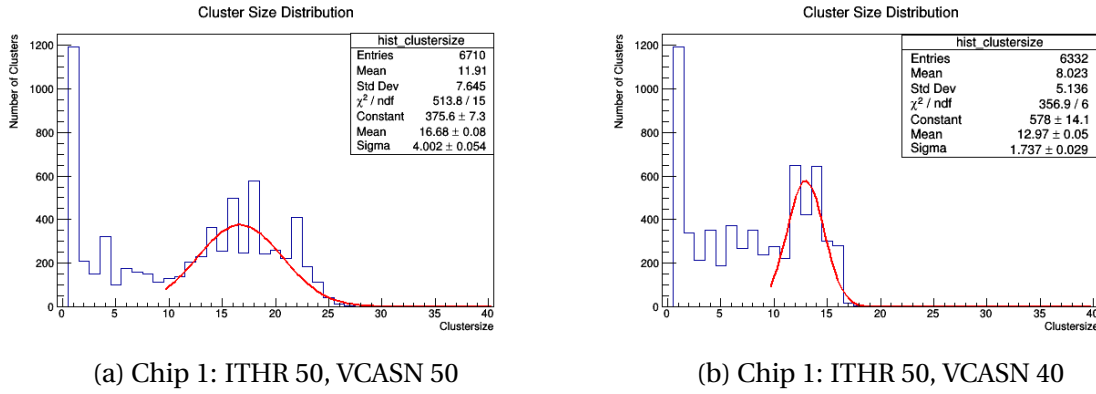
(a) Chip 1: ITHR 50, VCASN 50

(b) Chip 1: ITHR 50, VCASN 40

Figure 4.15: Cluster size distributions with Gauss fittings.

4.4.2 Results

From the cluster size distributions, it is clear that clusters are more likely to contain an even number of pixels than an odd number of pixels. This is likely a result of geometrical effects. It is most easily illustrated with a small cluster. If a small charge is deposited near the edge of a pixel it is likely to trigger a hit in two or four pixels depending on where it hits. It is, however, less likely to get a three-pixel hit. This geometric preference of even-numbered clusters appears to hold for larger clusters as well.

Both the mean and the standard deviation of the fitted Gaussian curves decreased with increasing threshold values. This can be seen in the cluster size distributions as the Gaussian curve's mean decreases, and the distributions get narrower squeezing in towards 10 pixels. It is assumed that all clusters with 10 pixels or more are made from alpha particles. Smaller clusters can come from noise, gammas or secondary particles.

The mean cluster size decreases with an increasing threshold for both chips, as seen in Figure 4.16. It appears that the slope of the curves for the two chips are approximately the same, but the curve for chip 2 lies above that of chip 1. The same tendency can be seen for the standard deviations in Figure 4.17.
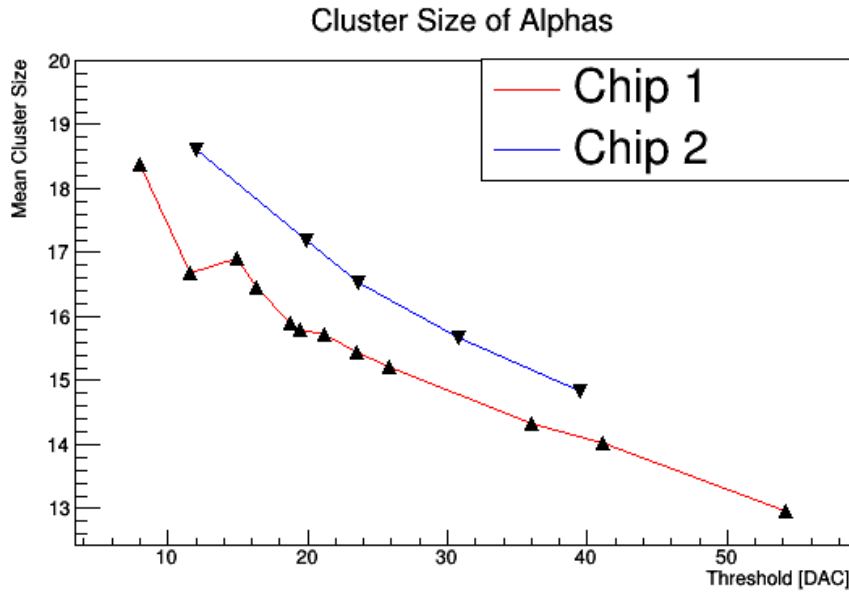
Figure 4.16: Mean cluster size of alphas for varying threshold of chip 1 and chip 2
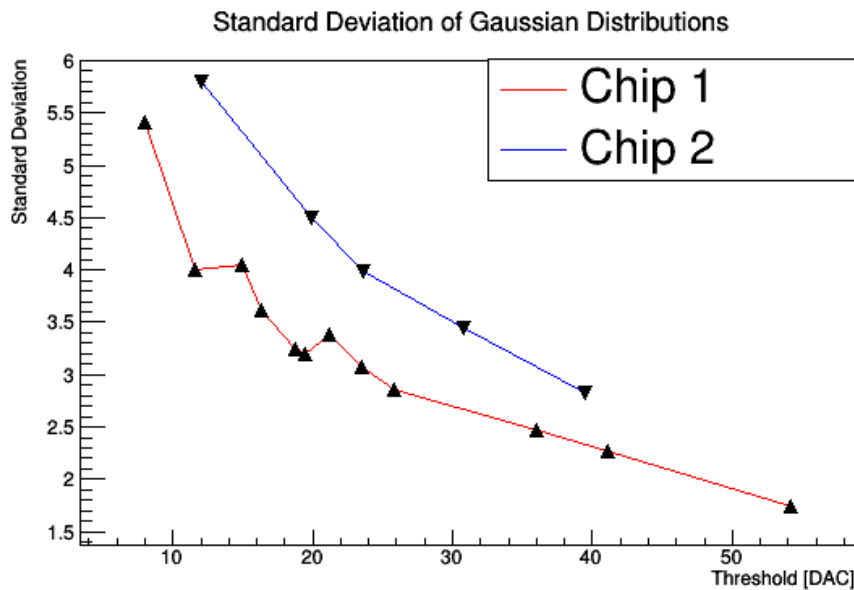

Figure 4.17: Standard deviation for varying threshold of chip 1 and chip 2

The threshold also affects the number of single-pixel hits, as seen in Figure 4.18. The number of single-pixel clusters is very high for low thresholds when no pixels are excluded. This number decreases rapidly with increasing threshold and then stabilises at about 1000 single pixel clusters per one million triggers for both chips. It appears that it stabilises for thresholds somewhere between 15 and 20 DAC. There is a high level of noise at low thresholds, as can be seen by the difference in the two curves for Chip 1 in Figure 4.18. Pixels that registered more than 100 hits were considered noisy. At higher thresholds the curves plateau, and the number of clusters from noise is reduced. This plateau is likely clusters made from the 60
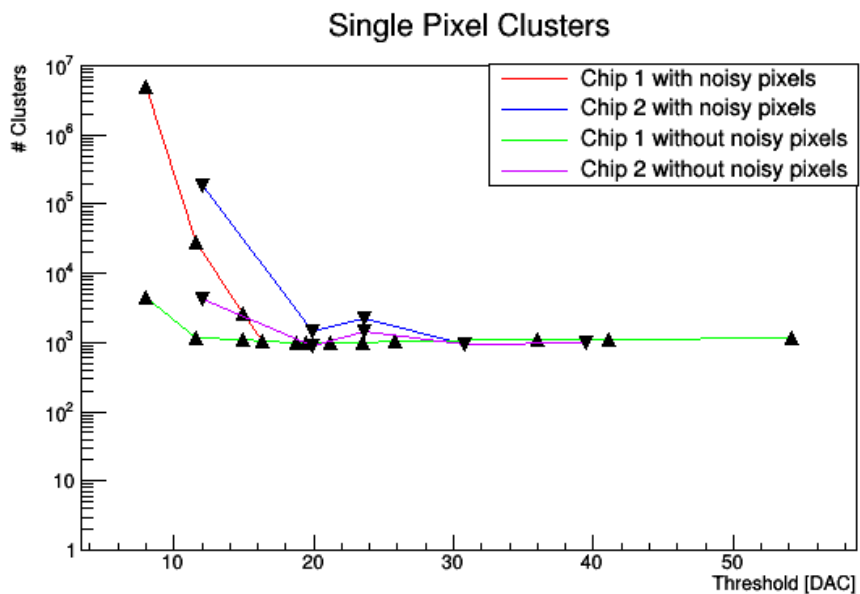
keV gammas.

Figure 4.18: Number of clusters with cluster size 1 for Chip 1 and 2 with and without hits from pixels firing more than 100 times.

Chapter 5

Characterisation of the ALPIDE with Electron and Carbon Ion Tracks

5.1 Electromagnetic Calorimeter with ALPIDE

Test-beam data was acquired with the EPICAL-2 prototype at the DESY (Deutsches Elektronen-Synchrotron) II test beam facility in February 2020. The setup used is explained in section 4.1.3. The calorimeter was irradiated with electron beams with energies ranging from 1 GeV to 5.8 GeV.

5.1.1 Preliminary Performance Results

The test-beam data has been used to estimate the energy response and energy resolution of the calorimeter prototype.

Only events with a single shower and minimal lateral leakage were analysed [32]. A shower from a one-electron event with a 5 Gev electron beam is shown in Figure 5.1.
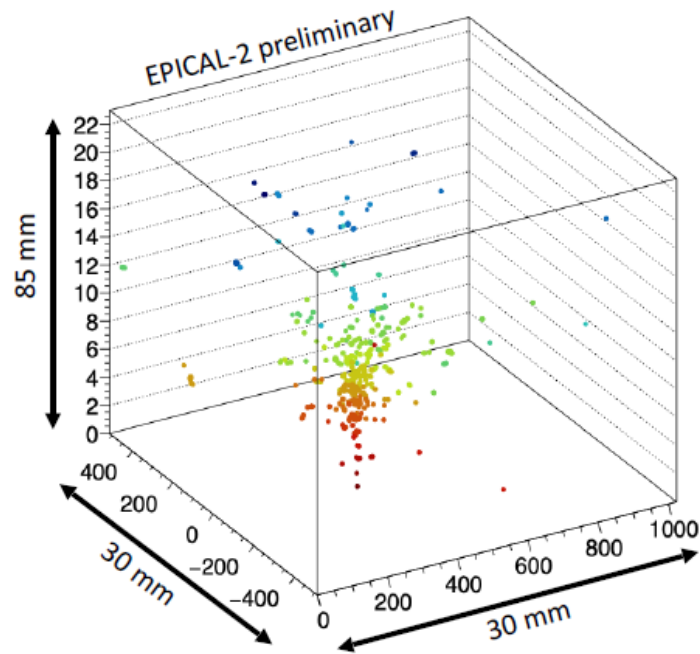
Figure 5.1: Evolution of electromagnetic shower in the EPICAL-2 prototype. The colour coding indicates layer [32]

The energy deposition in a calorimeter is proportional to the number of particles detected. The number of particles can be estimated by the number of pixel hits or the number of clusters. Figure 5.2 shows the number of pixel hits and clusters in events for different beam energies.
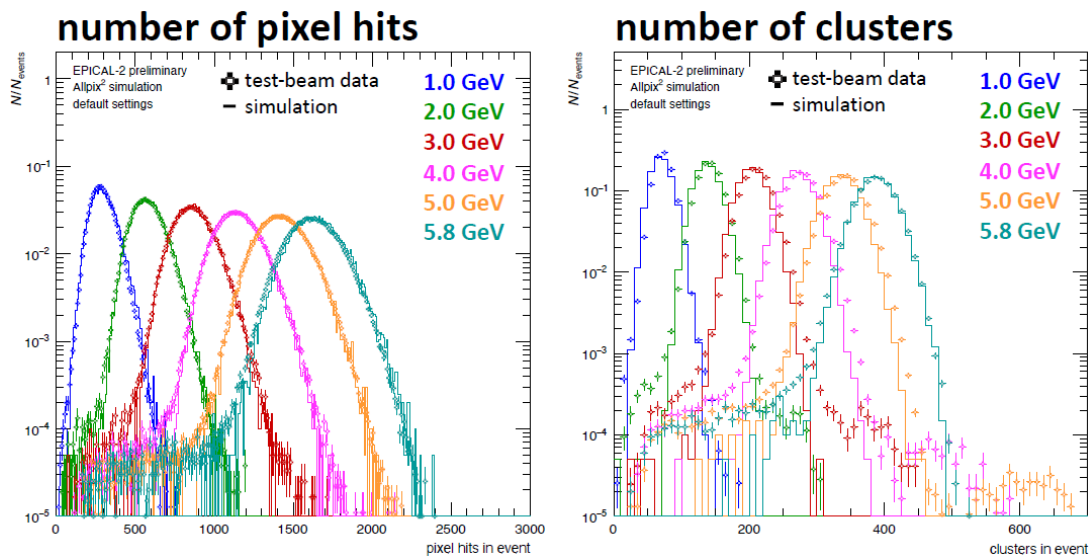

Figure 5.2: Number of hits and clusters in event [33]

The mean μ and standard deviation σ were extracted from the distributions in Figure 5.2

[33]. The means were used to evaluate the linearity of the energy response as seen in Figure 5.3.
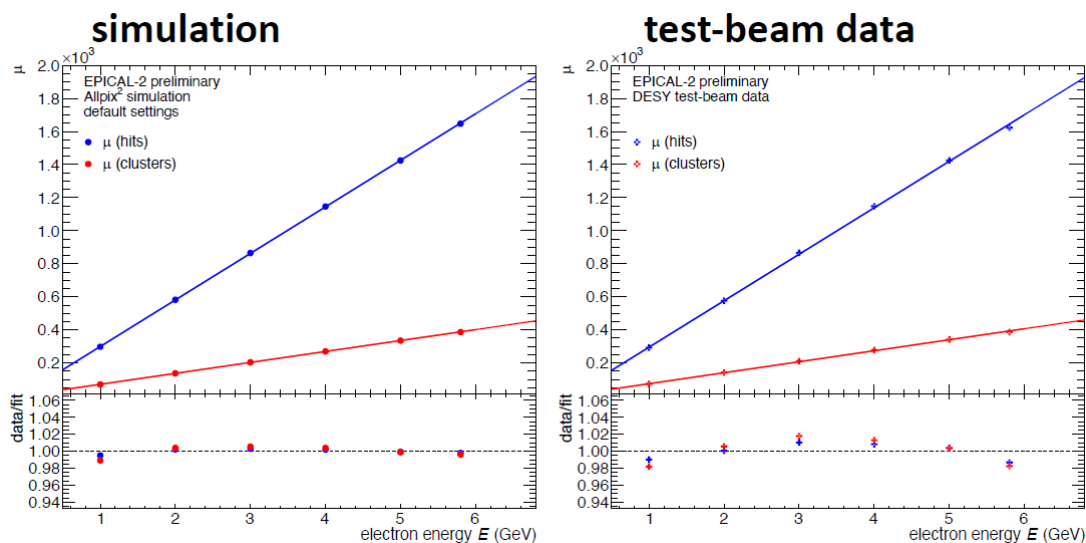

Figure 5.3: Energy response [33]

The energy resolution was evaluated by plotting σ/μ as seen in Figure 5.4. Using clusters gave better energy resolution than using pixel hits. [33]
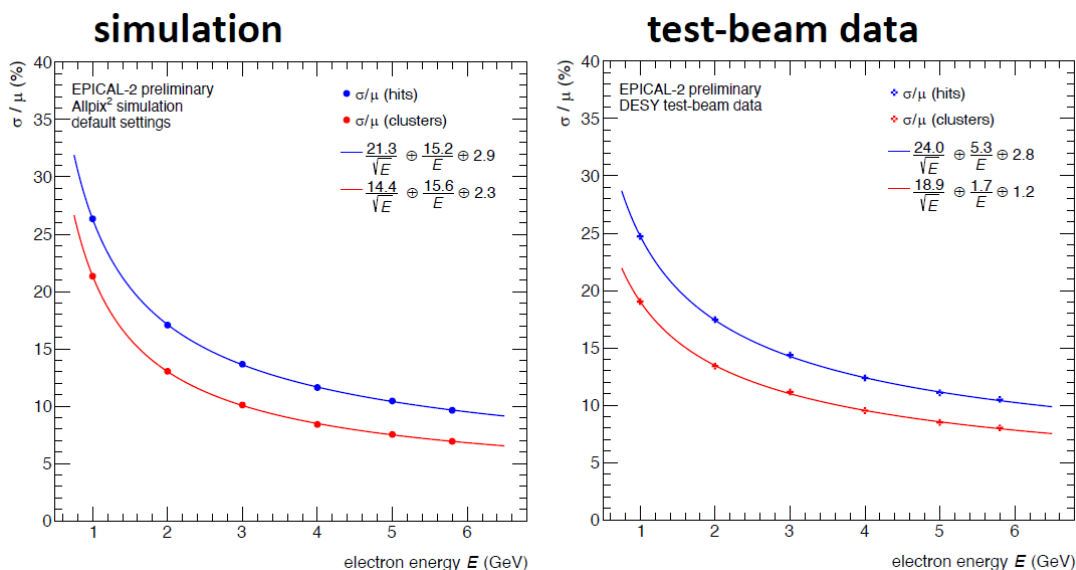

Figure 5.4: Energy resolution [33]

Large clusters with a tracklike structure has been observed in both test-beam data and simulations [7, 33]. The origin of these clusters is currently unknown. One possible explanation is that the electrons and positrons in the electromagnetic showers produce δ-electrons that travel in the epitaxial layer of the chips and make long tracks. In the following, large clusters in test-beam data taken with a 3 GeV electron beam will be analysed.

5.1.2 Analysis

Two separate beam runs are analysed in this section. For both runs, the electron beam had an energy of 3 GeV and was collimated by an internal collimator of 14 × 14 mm and a lead collimator of 12 × 12 mm. The data was taken with a 2μs strobe length. For the first run (Run_1305), the water cooling temperature was set to 25 °C, and 285 003 events were recorded. In the second run (Run_1358), the temperature was 30°C, and 522 000 events were recorded.

Two subsequent hits were identified as part of the same cluster if the difference in the x-position was less than 3 and the difference in y-position was less than 5. Only clusters with more than 10 pixels are analysed.

Examples of large clusters can be seen in Figures 5.5 and 5.6. Figure 5.5 shows clusters with 30-50 pixels while Figure 5.6 shows clusters containing more than 50 pixels.
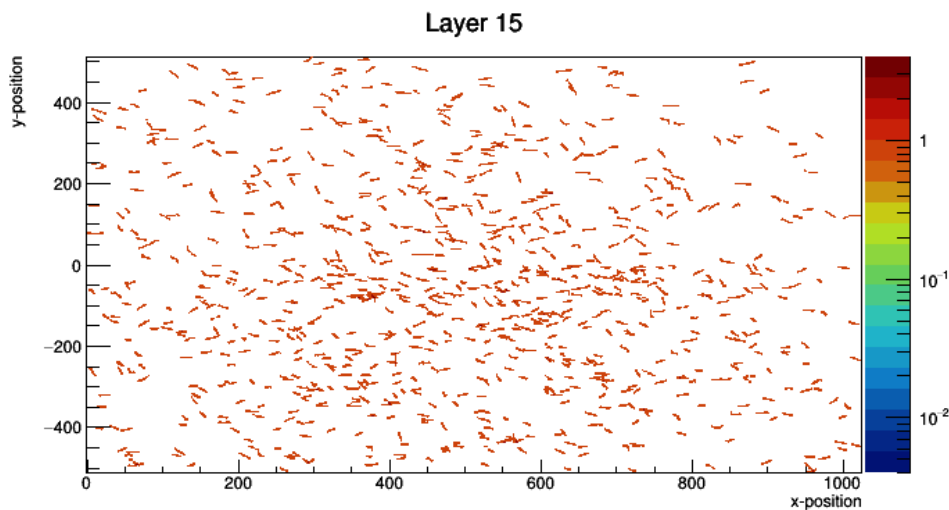

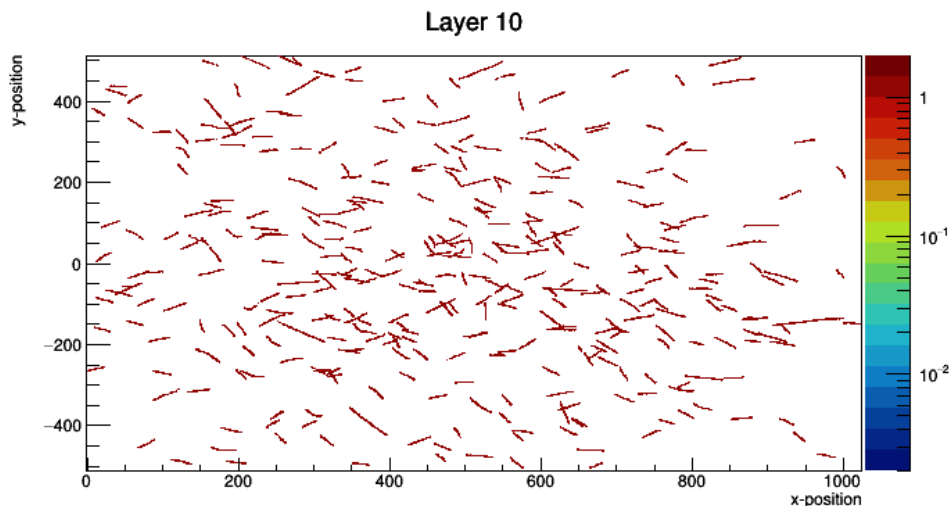Figure 5.5: Hit map of clusters with cluster size between 30 and 50 pixels in layer 15 for Run_1305

Figure 5.6: Hit map of clusters with cluster size larger than 50 pixels for Run_1305

Assuming that the tracks are straight, Pythagoras was used to find the length of the tracks. The maximum and minimum value of both x and y positions was identified for each identified cluster. The length given in pixels was then defined as

$$\text{length [pixels]} = \sqrt{(x_{max} - x_{min})^2 + (y_{max} - y_{min})^2}$$

In order to find the length of the tracks in mm, the pixel size (29.24 μm $\times$ 26.88 μm) was implemented. The length in mm was then found as

$$\text{length [mm]} = \frac{\sqrt{((x_{max} - x_{min}) \cdot 29.24)^2 + ((y_{max} - y_{min}) \cdot 26.88)^2}}{1000}$$

In the following, it is assumed that the tracks are made from δ-electrons travelling in the silicon layer of the ALPIDE chip. The range of the electrons in silicon can then be found by multiplying the length of the tracks (in cm) with the density of silicon (2.33 g/cm^3).

The range was converted to kinetic energy by matching the required kinetic energy to the CSDA range in the ESTAR database [34].

5.1.3 Results

The cluster size distributions of clusters with more than 10 pixels can be seen in Figure 5.7. The number of clusters decreases sharply with increasing cluster sizes. The slope appears to be slightly sharper for Run_1305 than for Run_1358. Run_1358 also includes larger cluster sizes than Run_1305.
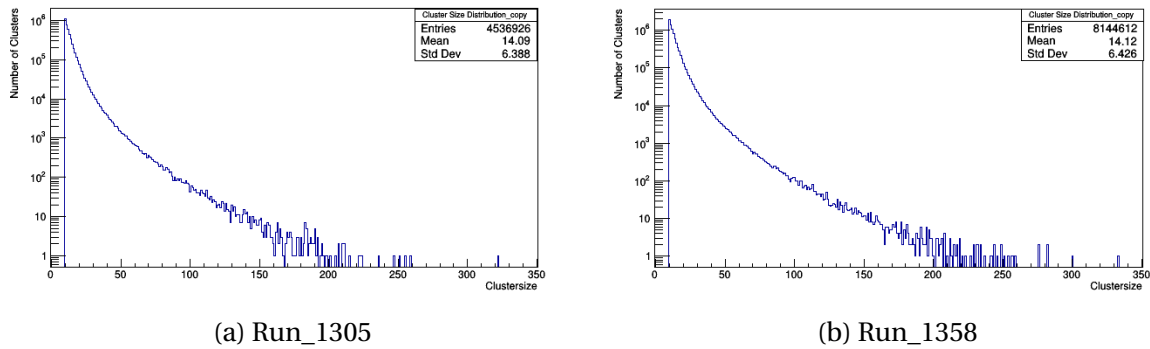
(a) Run_1305

(b) Run_1358

Figure 5.7: Cluster size distributions.

Figures 5.8 and 5.9 shows the normalised track length distributions for the two runs. The red lines show track length for all layers in the EPICAL-2, and the blue lines show track lengths for only the first two layers.
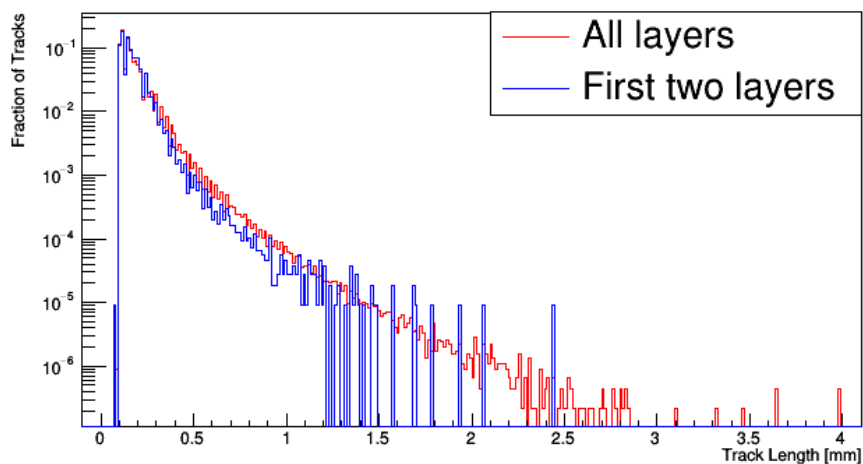

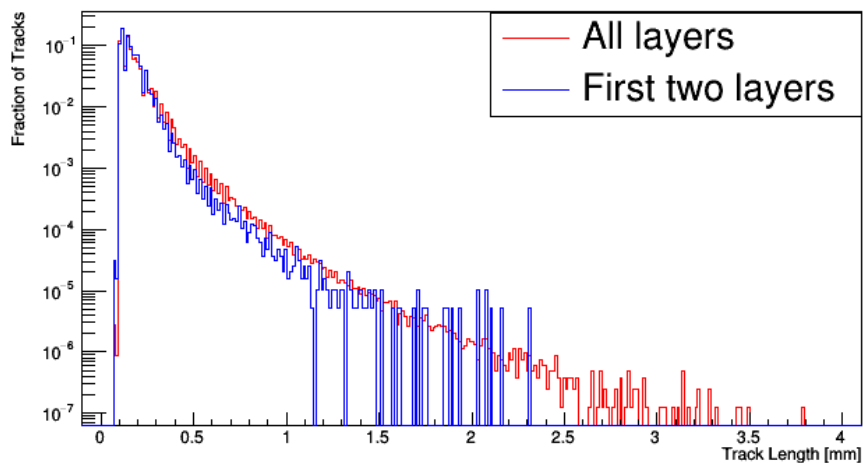Figure 5.8: Track length distributions for all and first two layers for Run_1305

Figure 5.9: Track length distributions for all and first two layers for Run_1358

For both runs, the first two layers do not contain any tracks longer than 2.5 mm. When all layers are considered, tracks with lengths up to 4 mm are recorded. In the further layers, the electromagnetic showers are fully developed and the number of particles is significantly larger than in the first two layers. In the further layers the spread in the impact angle of the electrons and positrons increases.

The distributions of the calculated electron energies can be seen in Figures 5.10 and 5.11.
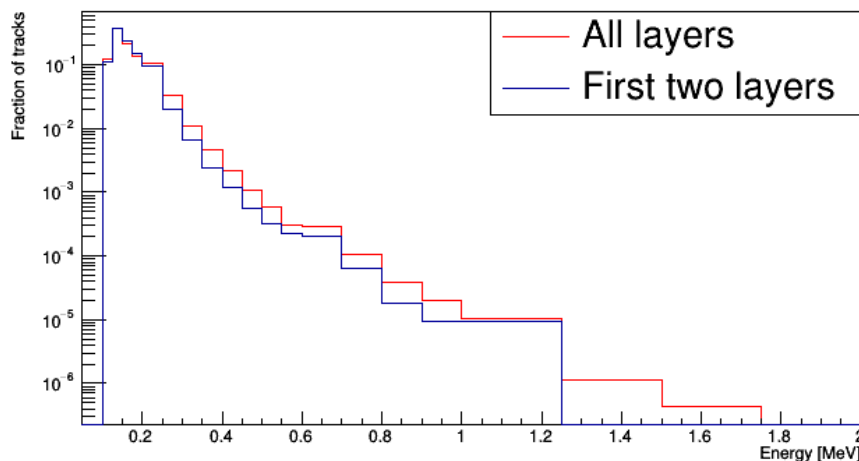
Figure 5.10: Energy distributions for all and first two layers for Run_1305
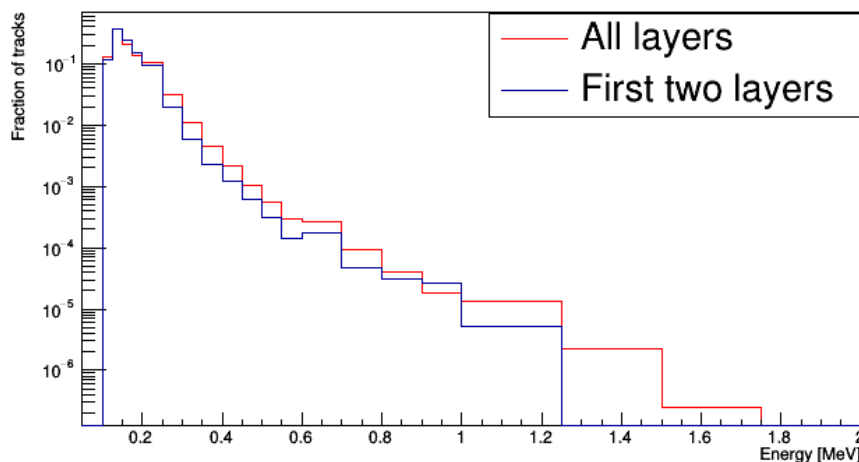
Figure 5.11: Energy distributions for all and first two layers for Run_1358

For both runs, the highest recorded energy is about 1.6 MeV when all layers are taken into account and 1.2 MeV for the first two layers.

For an electron beam with an energy of 3 GeV, it is expected that the maximum energy it can transfer to a δ-electron in a single collision is 1.5 GeV. It appears that all tracks correspond to energies far below this energy.

Figure 5.12 shows the energy distribution from Figure 5.11 with a logarithmic energy scale. The shape of the energy distributions in 5.12 closely resembles the theoretic δ-electron curves in Figure 2.5. The slope of the measured energy spectra is, however, significantly steeper than the theoretical. The curve from the first two layers lies below the curve for all layers. From the theoretic spectra we can see that this might indicate that the particles producing δ-electrons in the first layers have slightly higher energy than in all layers.
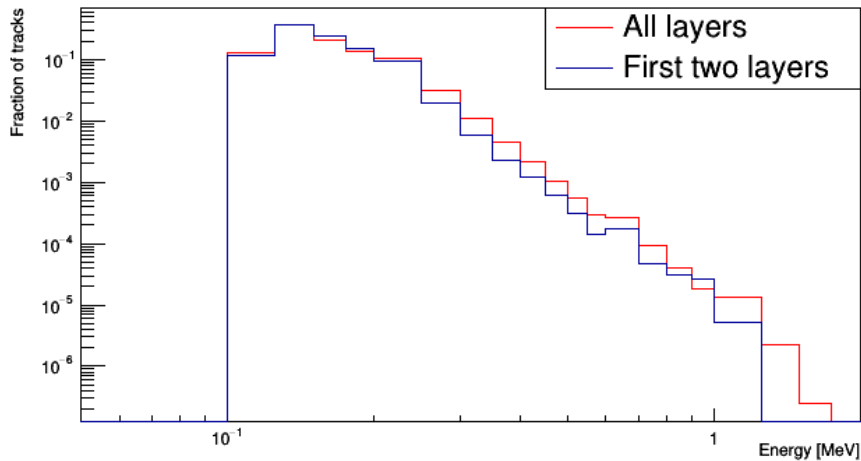
Figure 5.12: Energy distributions for all and first two layers for Run_1358 with logarithmic energy scale

5.2 Carbon Ion Tracks in ALPIDE

The data analysed in this section was collected during beam tests at the Heidelberg Ion-Beam Therapy Center (HIT) in December of 2018.

A single ALPIDE was mounted on an aluminium flex cable. It was connected to a custom made transition card (JODY board) via a ZIF connector. The transition card was responsible for the power delivery to the ALPIDE chip and acted as an intermediate between the ALPIDE chip and the readout unit (VCU118). The readout unit communicated with the Central Processing Unit (CPU) via a 1 m samtec firefly cable. Figure 5.13 shows a schematic of the setup.

Figure 5.13: Experimental setup

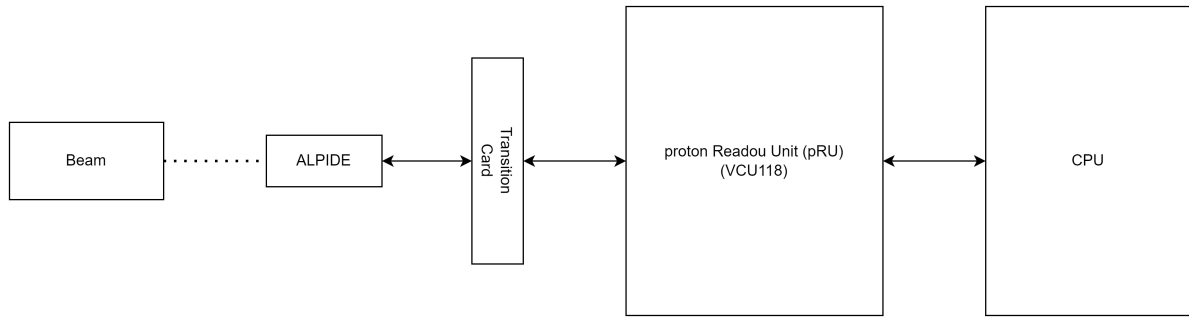Lateral scans were conducted with carbon and helium. The ALPIDE chip was placed longitudinally with respect to the beam so that particles would enter the ALPIDE chip on the short side as seen in Figure 5.14. The strobe length was set to 485 μs.
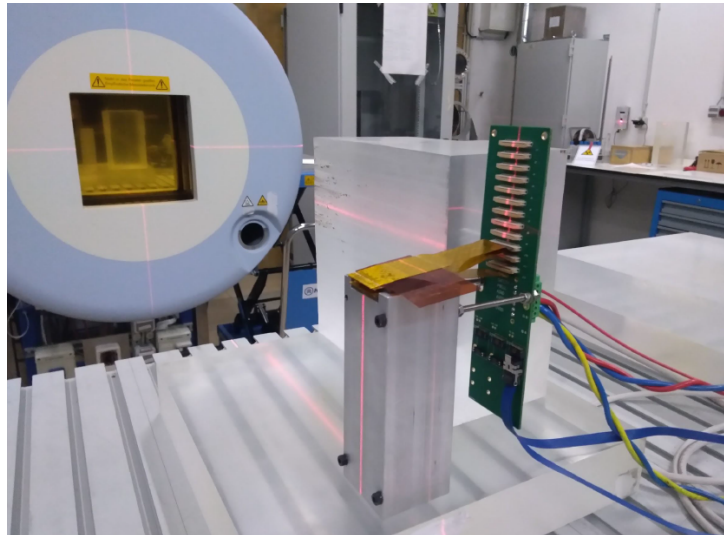
Figure 5.14: Picture of the experimental setup for lateral scans.

An overview of the runs analysed in this section can be seen in Table 5.1. The expected range (in g/cm^2) of the particles in silicon was found from online tables [31, 35]. The approximate range in cm was found by dividing the range by the density of silicon (2.33 g/cm^3).

Run Number	Particle	Beam Energy [MeV/u]	Events	Range in Si [cm]
141218_235056	Carbon	140.4	408	2.53
151218_0209	Helium	75.39	4952	2.55
151218_04237	Carbon	140.4	4960	2.53

Table 5.1: Beam particles and energies for runs used in analysis

5.2.1 Analysis

The goal of the analysis is to identify tracks from beam particles and investigate the microstructure of these tracks. For a track to be analysed, it should have a significant length and be fairly straight and aligned with the chip.

Only events with at least 1000 hits are analysed to ensure that the events contain tracks. A hit map for a single event can be seen in Figure 5.15. The tracks in this event are fairly straight and aligned with the chip. Some of the tracks also appear to come from particles that travel a considerable length in the epitaxial layer of the chip. However, some of the tracks are very close together, which makes them difficult to distinguish.

By projecting the y-values of all the hits in an event into a 1D histogram the particle tracks make clear peaks as seen on the right in Figure 5.15. These peaks are used to identify the centre of tracks. To qualify as a track centre, the y-position must contain at least 150 pixel hits. This constraint is set to avoid registering very short tracks and tracks from particles that do not travel fully in the epitaxial layer. y-positions are considered for track centres if the next y-value contains fewer hits. To avoid registering several centre values for the same track it is required that the y-position is at least 10 pixels away from the previous centre value. For the event shown in Figure 5.15 a total of 10 centre values are identified using these requirements.
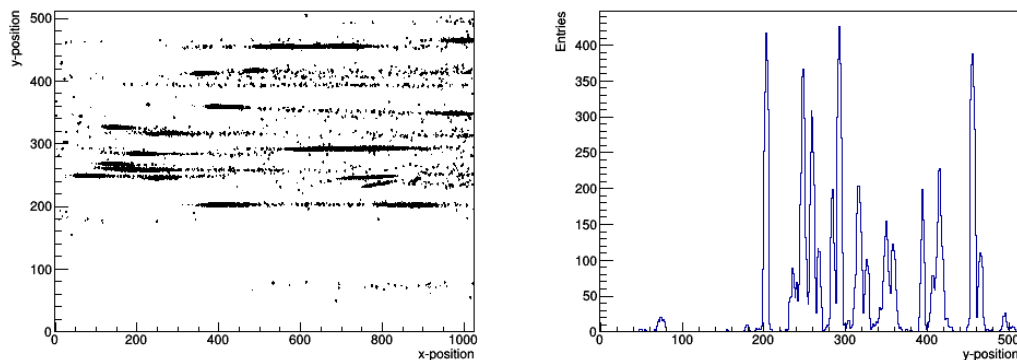
Figure 5.15: On the left is the hit map for a single event ID. On the right is the corresponding hits per y-position.

Once all track centres in an event ID are identified, pixel hits that are less than 15 pixels from a track centre are identified as part of this track if it is not closer to another centre. This limitation of distance from track centre is set to avoid registering too many hits from noise, small clusters and unidentified tracks. However, it is kept large enough that pixels belonging to tracks hitting the chip at a small angle can still be identified. Figures 5.16 and 5.17 show hit maps before and after track identifying.

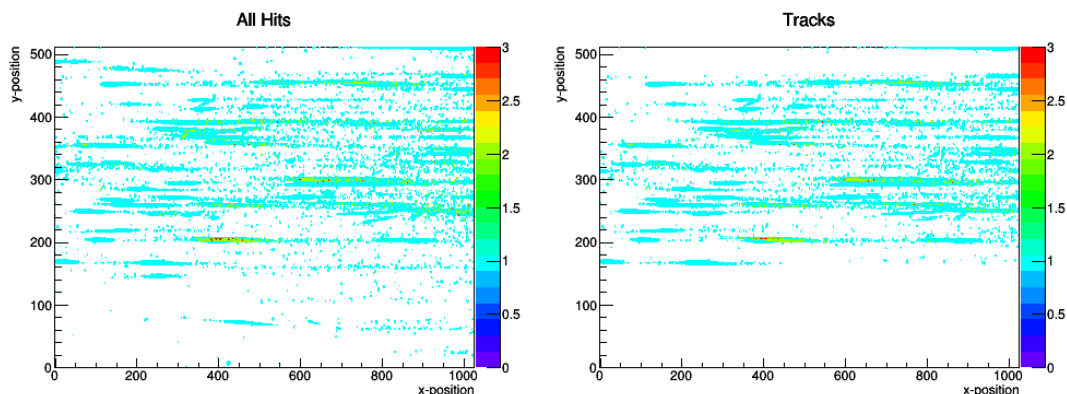Figure 5.16: Hit map of run 141218_235056 containing all registered hits from event IDs with more than 1000 hits is on the left. On the right is the corresponding hit map for the identified tracks.

Figure 5.17: Cropped hit map with y-positions 0-150 of run 151218_0209 containing all registered hits from event IDs with more than 1000 hits is on the left. On the right is the corresponding hit map for the identified tracks.
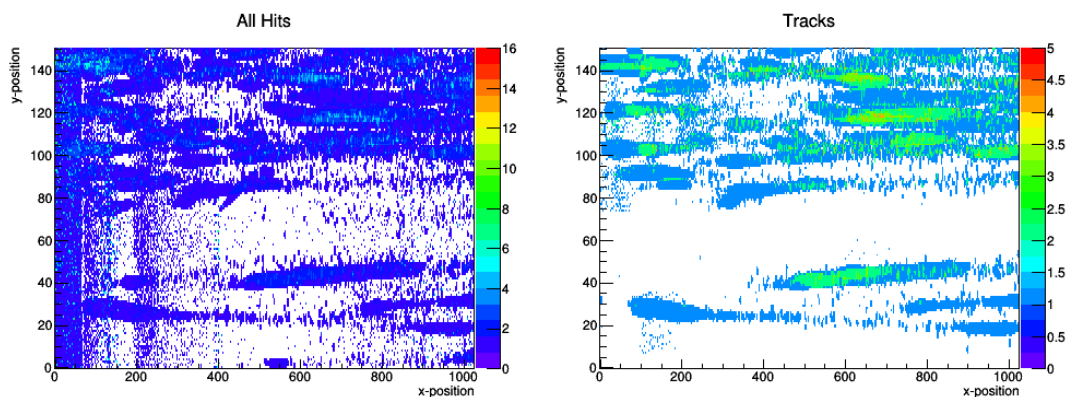
In Figures 5.16 and 5.17 it can be seen that a lot of noise and short tracks are filtered out when identifying tracks. This is particularly seen in Figure 5.17 where there is a lot of noise at low x-positions in the original hit map and much less noise in the hit map only containing identified tracks.

For each identified particle track, the width of the track is examined for all x-values. Looping over all x-values, the maximum and minimum y-values are saved if they are part of a track with at least four consecutive pixels with registered hits in the y-direction. This requirement is added to avoid registering noise or small clusters close to the track as part of the track. The width of the track at the given x-value is then identified as width = $y_{max} - y_{min} + 1$.

5.2.2 Results

Figure 5.18 shows a few particle tracks from carbon ions. These tracks are relatively straight and long.
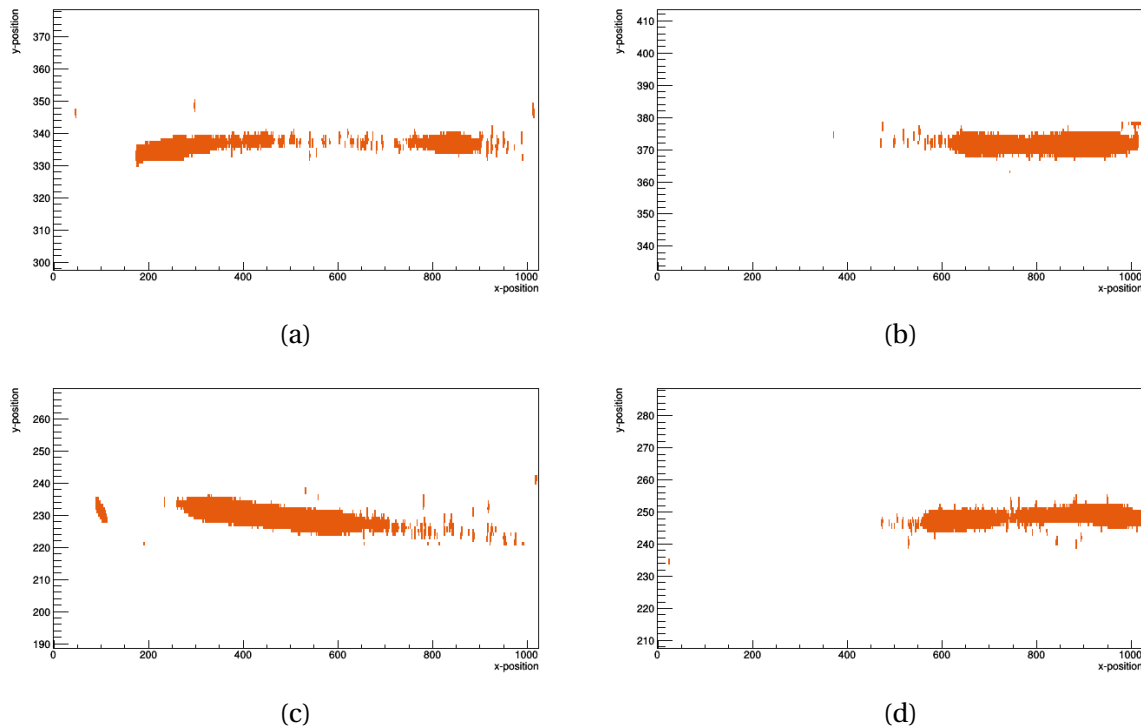

(a)

(b)

(c)

(d)

Figure 5.18: Single particle tracks from carbon ions

In Figure 5.18a the particle appears to move in and out of the epitaxial layer of the ALPIDE chip as parts of the track are broken up. The tracks in Figure 5.18b and 5.18d start at the edge of the chip, but start to break up after about 500 pixels where the carbon ion probably exits the epitaxial layer. In Figure 5.18c the particle appears to gradually enter the epitaxial layer of the chip and travel fully in the epitaxial layer from x-position around 700 to around 300.

The particle tracks in Figure 5.18 show some thin lines perpendicular to the main particle tracks. This is particularly seen in Figure d. These thin lines may be made from δ-electrons.

Figure 5.19 shows all pixels identified as part of a track with their x-position and distance from track centre for the helium beam. Figure 5.20 shows the same for carbon.
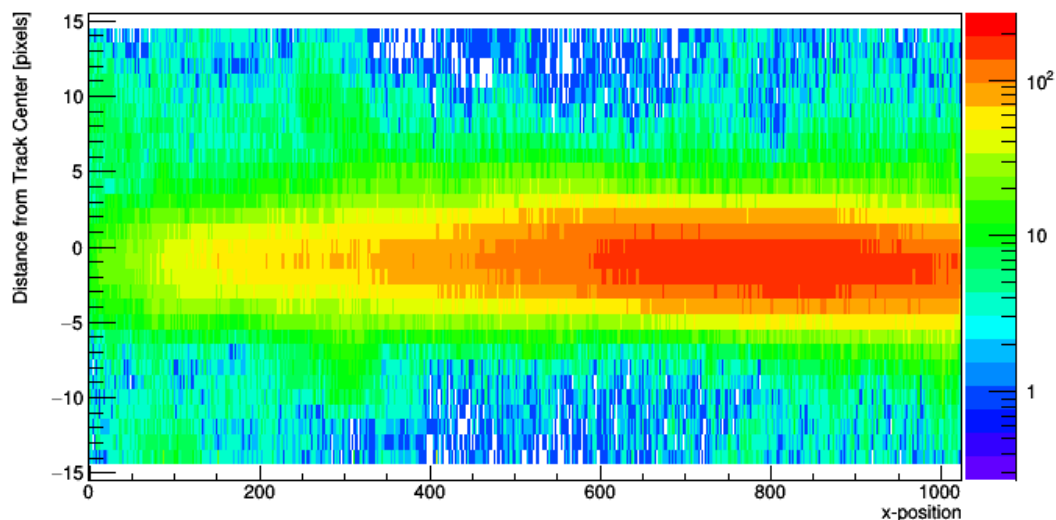
Figure 5.19: All hits identified as part of a track plotted with their x-position and distance from track centre for helium (run 151218_0209)

It appears that the density of tracks is highest between x-positions of 600 and 1000. This shows that many particles making tracks in the chip do not enter at x = 1023. The mean y-value of the plot is -0.8, this might indicate that the algorithm for finding track centres slightly overestimates the position of the centres.

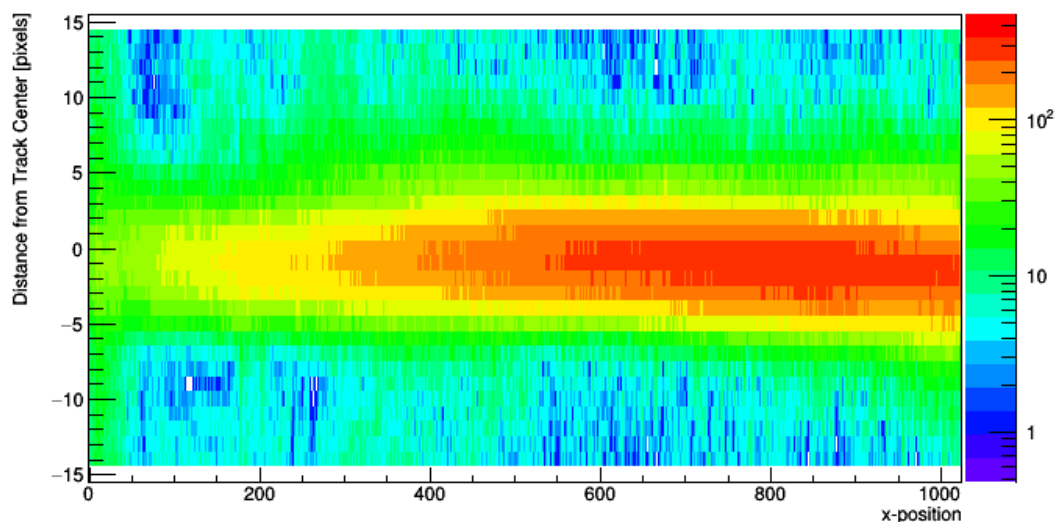Figure 5.20: All hits identified as part of a track plotted with their x-position and distance from track centre for carbon (run 151218_04237)

For the carbon beam, the track density appears to be similar to that of helium. We can, however, observe some more noise at low x-positions. This noise is in the same region as we can see on the left in Figure 5.17. In Figure 5.17 this noise is successfully filtered out,

likely due to the noise occurring in events without tracks. If the noise occurs in an event with particle tracks, it will likely appear as in Figure 5.20. It appears that the carbon tracks are a little longer than the helium tracks.

Figure 5.21 shows the distribution of the identified track widths for both the helium and the carbon beam. Due to the noise seen at low x-positions, widths at x-positions below 100 are not included in the distributions.
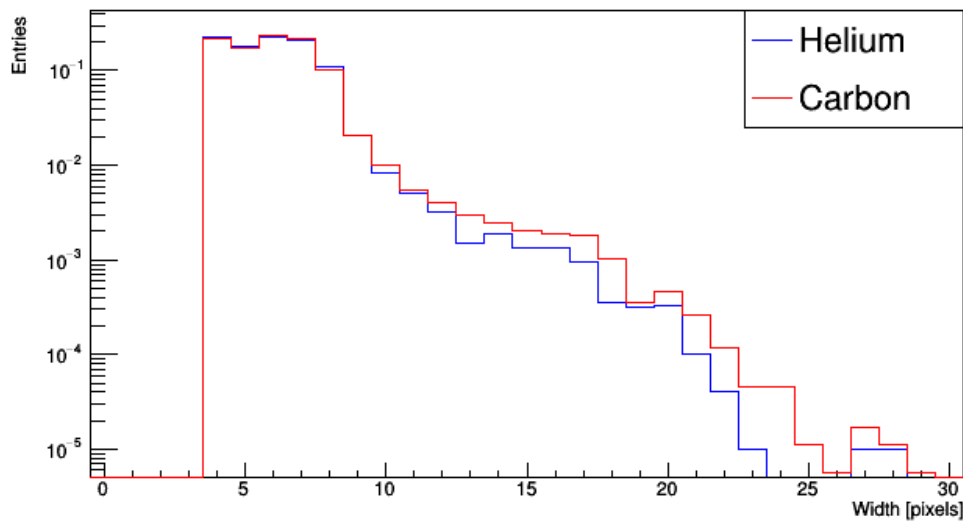

Figure 5.21: Normalised width distributions for helium (run 151218_0209) and carbon (run 51218_04237)

The majority of the identified widths lie between 4 and 8 pixels for both helium and carbon. These widths are likely due to charge diffusion from primary ionisation. There is a sharp drop-off in widths above 8 pixels. The larger widths can come from δ-electrons, pixel hits from unidentified particle tracks or noise. The curve decreases more rapidly for the helium beam than for the carbon beam.

Assuming that all widths are a product of δ-electrons an energy distribution can be found. The range of the electrons is found by multiplying the width in cm with the density of silicon (2.33 g/cm^3). Energy values from the ESTAR database are then matched to these ranges. The resulting energy distribution can be seen in Figure 5.22. Around the range of 200-300 keV the shape of the energy distribution resembles a δ-electron spectrum. Below this range the distribution is dominated by the widths from the primary ionisation and above the range we run out of data points.
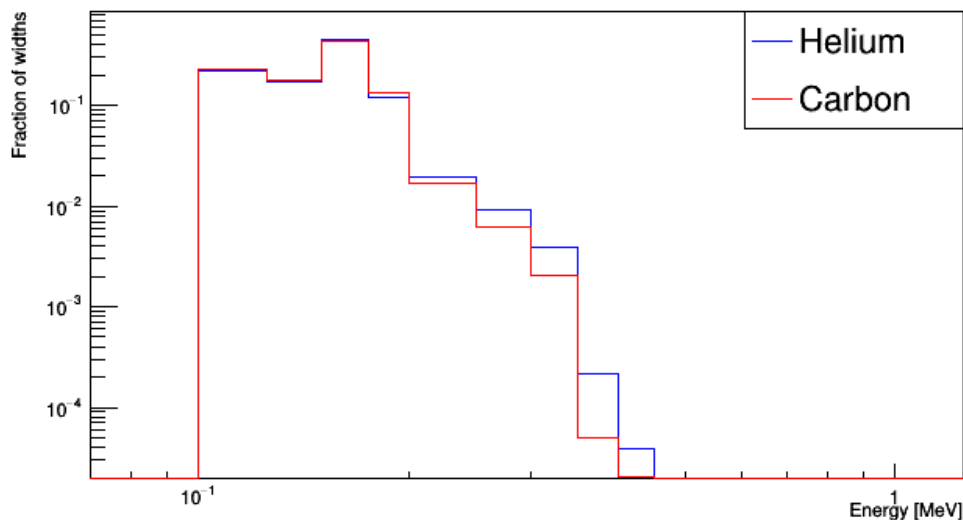
Figure 5.22: Normalised energy distributions for helium (run 151218_0209) and carbon (run 51218_04237)

Figures 5.23 and 5.24 show the average track widths for all x-positions for helium and carbon, respectively. A running average filter was added to even out fluctuations. Values from the five previous and following x-positions were used in the running average.
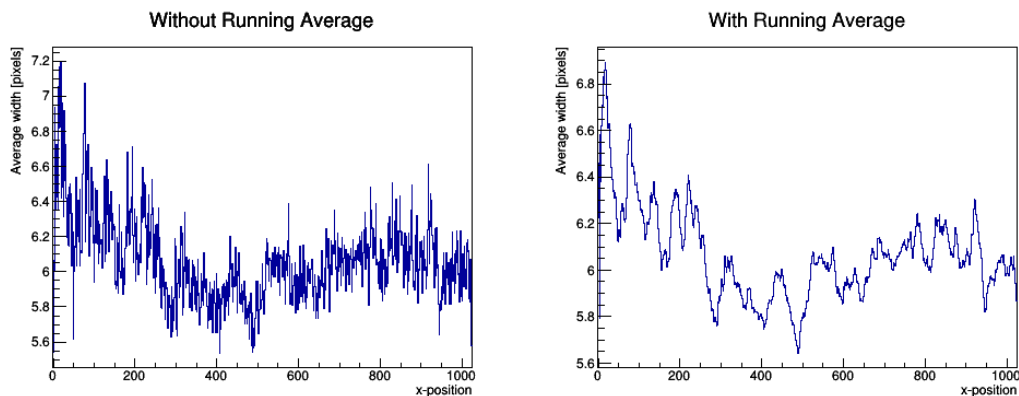

Figure 5.23: Average track width along the x-direction for helium (run 151218_0209)
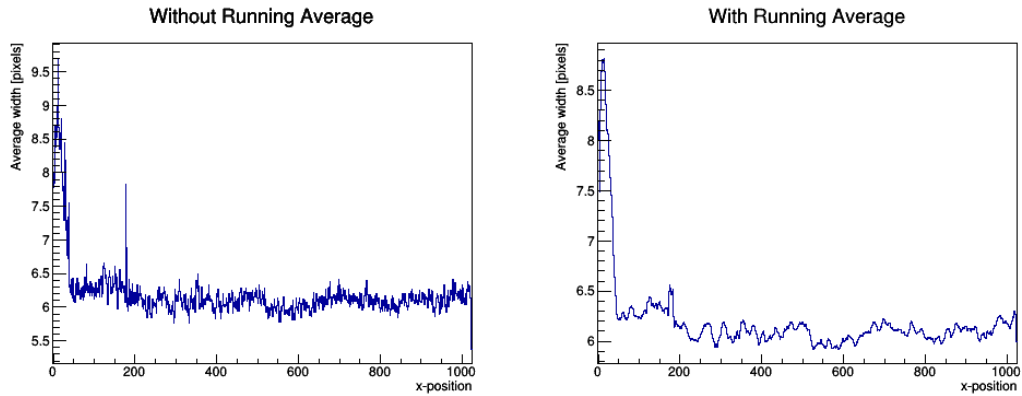
Figure 5.24: Average track width along the x-direction for carbon (run 151218_04237)

The average widths of the tracks along the x-position appears to be relatively stable for x-positions 200-1000 for the carbon beam and about 250-1000 for the helium beam. In these ranges the widths are likely dominated by the incident beam particles. At the lower x-positions the widths might be dominated by secondary particles with longer ranges. For the carbon beam, the noise at the left side of the chip is visible as a sharp increase in the average width below x-position 50. Based on the ranges listed in Table 5.1 the helium beam would stop around x-position 150 and the carbon beam around x-position 160. These ranges do not take into account the distance travelled in air before the beam enters the silicon, so the actual range is a little shorter. It is therefor likely that the beams stop around x-positions 200/250 as indicated by the change in average width.

Chapter 6

Conclusion

Ideally, all chips in the final pCT system should have the same charge threshold. To achieve a uniform response, the charge threshold of each chip will need to be calibrated. The threshold can be adjusted by changing the ITHR and VCASN settings. As seen in section 4.2 lowering the VCASN value strongly increases the charge threshold. Increasing ITHR also increases the threshold, but the change is not as rapid as for VCASN. Although the general effect of changing VCASN and ITHR is the same for all chips, the threshold curves differ quite a lot. This difference in the curves complicates calibration of threshold as a given change in VCASN or ITHR does not give the same change in threshold for all chips. It would be interesting to repeat these tests for chips on a 9-chip string.

In section 4.3 it was found that the charge threshold has a large impact on the fake-hit rate of the ALPIDE. With changing ITHR values the response of the different chips was relatively uniform with an exponential rise in FHR with lowering ITHR values. The FHR also increased with increasing VCASN values. Here there was a larger spread in the curves for different chips.

The strobe length also affects the noise level. A linear relationship was found between the strobe duration and the fraction of frames that registered hits.

In section 4.3.3 it was found that masking very noisy pixels is an effective way to reduce the amount of data from the system when no ionising radiation is present. It was calculated that by masking only the pixels that fire in more than 90% of triggers the data rate for the final pCT system could be lowered from 27.4 Gbit/s to 9.77 Gbit/s. By lowering the masking threshold to 1% the data rate could be further reduced to 1.29 Gbit/s. Based on the data this would involve masking less than one pixel per chip.

The cluster size may be used as an indicator for how much energy was deposited in the chip. Particles passing through the DTC in the pCT system will generate large clusters as they reach

their Bragg peak. The information of cluster size can be used to improve the accuracy when calculating the energy of the outgoing particle. From the results in section 4.4 we can see that an increase in threshold gives a decrease in cluster size and the spread in cluster size. We also see that some pixels produce more noise when the threshold is low.

Data from the EPICAL-2 prototype with an electron beam was analysed in section 4.1.3. Many long tracks were identified in the ALPIDE chips. Assuming that the tracks were made from electrons depositing all their energy in the chip, the distribution of the initial energies was found. The maximum energy in these distributions was about 1.6 MeV which is far below the theoretical maximum energy of 1.5 GeV that a 3 GeV electron can transfer to a δ-electron. The shape of the energy distributions resembles the shape of energy spectra for δ-electrons.

In section 5.2 the microstructure of particle tracks from carbon and helium ions was investigated. The tracks had a typical width of 4-8 pixels. These widths are probably made from the charge diffusion of the primary ionisation from the particles. A distribution of larger widths up to about 25 pixels is also observed. These larger widths can be the product of δ-electrons. With a stack of many thinned ALPIDEs it seems to be possible to study microscopic ionisation processes along ion beams as they traverse the detector.

Bibliography

[1] P. Mayles, A. Nahum, and J. C. Rosenwald. *Handbook of Radiotherapy Physics: Theory and Practice*. Baton Rouge: Baton Rouge: CRC Press, 2007. ISBN: 0750308605,9780750308601. DOI: 10.1201/9781420012026.

[2] Ervin B. Podgorsak. *Radiation Physics for Medical Physicists*. 3rd ed. 2016. Graduate Texts in Physics. Cham: Cham: Springer International Publishing, 2016. ISBN: 1868-4513 9783319253800,3319253808. DOI: 10.1007/978-3-319-25382-4.

[3] William R. Leo. *Techniques for nuclear and particle physics experiments : a how-to approach*. 2nd rev. ed. Berlin: Springer, 1994. ISBN: 3540572805,0387572805.

[4] Stefaan Tavernier. *Experimental Techniques in Nuclear and Particle Physics*. Berlin, Heidelberg: Berlin, Heidelberg: Springer Berlin / Heidelberg, 2010. ISBN: 9783642008283,3642008283.

[5] Faiz M. Khan and John P. Gibbons. *Khan's the physics of radiation therapy*. Fifth edition. Physics of radiation therapy. Philadelphia, Pennsylvania: Wolters Kluwer, 2014. ISBN: 9781451182453.

[6] Lucio Cerrito. *Radiation and Detectors: Introduction to the Physics of Radiation and Detection Devices*. Graduate Texts in Physics. Cham: Cham: Springer International Publishing, 2017. ISBN: 1868-4513 3319531794,9783319531793. DOI: 10.1007/978-3-319-53181-6.

[7] Emilie Haugland Solheim. "Characterisation of a Digital Sampling Calorimeter Prototype for Proton Computed Tomography With Electron Beams". MA thesis. UiB, des 2020. URL: https://hdl.handle.net/11250/2720436.

[8] A. Akkerman, M. Murat, and J. Barak. "Delta-electron spectra, inelastic cross sections, and stopping powers of ions in silicon: Comparison between different models". In: *Nuclear instruments methods in physics research. Section B, Beam interactions with materials and atoms* 321 (2014), pp. 1–7. ISSN: 0168-583X. DOI: 10.1016/j.nimb.2013.12.002.

[9] Cecile Bopp. "The proton as a dosimetric and diagnostic probe". Thesis. 2014.

[10] Thomas E. Johnson and Herman Cember. *Introduction to health physics.* Fifth edition. New York: McGraw-Hill Education, 2017. ISBN: 9780071835275,9780071835268.

[11] Andreas Tefre Samnøy. "Characterization and application of 3D silicon microdosimeters". Thesis. 2020.

[12] Peter Hoskin. *External Beam Therapy.* Oxford, UNITED KINGDOM: Oxford University Press, Incorporated, 2012. ISBN: 9780191649646. URL: http://ebookcentral.proquest.com/lib/bergen-ebooks/detail.action?docID=998976.

[13] Radhe Mohan and David Grosshans. "Proton therapy – Present and future". In: *Adv Drug Deliv Rev* 109 (2017), pp. 26–44. ISSN: 0169-409X. DOI: 10.1016/j.addr.2016.11.006.

[14] Christian P. Karger and Peter Peschke. "RBE and related modeling in carbon-ion therapy". In: *Phys. Med. Biol* 63.1 (2017), 01TR02. ISSN: 0031-9155,1361-6560. DOI: 10.1088/1361-6560/aa9102.

[15] Nadine Barrie Smith and Andrew Webb. *Introduction to medical imaging : physics, engineering and clinical applications.* Cambridge texts in biomedical engineering. Cambridge: Cambridge University Press, 2011. ISBN: 9780521190657.

[16] Ming Yang et al. "Comprehensive analysis of proton range uncertainties related to patient stopping-power-ratio estimation using the stoichiometric calibration". In: *Phys. Med. Biol* 57.13 (2012), pp. 4095–4115. ISSN: 0031-9155. DOI: 10.1088/0031-9155/57/13/4095.

[17] B. Li et al. "Comprehensive analysis of proton range uncertainties related to stopping-power-ratio estimation using dual-energy CT imaging". In: *Phys. Med. Biol* 62.17 (2017), pp. 7056–7074. ISSN: 0031-9155,1361-6560. DOI: 10.1088/1361-6560/aa7dc9.

[18] Johan Alme et al. "A High-Granularity Digital Tracking Calorimeter Optimized for Proton CT". In: *Frontiers in physics* 8 (2020). ISSN: 2296-424X. DOI: 10.3389/fphy.2020.568243.

[19] George Dedes et al. "Experimental comparison of proton CT and dual energy x-ray CT for relative stopping power estimation in proton therapy". In: *Phys. Med. Biol* 64.16 (2019), pp. 165002–165002. ISSN: 0031-9155,1361-6560. DOI: 10.1088/1361-6560/ab2b72.

[20] Leonardo Rossi et al. *Pixel Detectors: From Fundamentals to Applications.* Particle Acceleration and Detection. Berlin, Heidelberg: Berlin, Heidelberg: Springer Berlin / Heidelberg, 2006. ISBN: 3540283323,9783540283324.

[21] R. Turchetta et al. "CMOS Monolithic Active Pixel Sensors (MAPS): New 'eyes' for science". In: *Nuclear instruments & methods in physics research. Section A, Accelerators, spectrometers, detectors and associated equipment* 560.1 (2006), pp. 139–142. ISSN: 0168-9002. DOI: `10.1016/j.nima.2005.11.241`.

[22] W. Snoeys. "CMOS monolithic active pixel sensors for high energy physics". In: *Nuclear instruments & methods in physics research. Section A, Accelerators, spectrometers, detectors and associated equipment* 765 (2014), pp. 167–171. ISSN: 0168-9002. DOI: `10.1016/j.nima.2014.07.017`.

[23] Lukasz Maczewski. "Measurements and simulations of MAPS (Monolithic Active Pixel Sensors) response to charged particles - a study towards a vertex detector at the ILC". In: (2010).

[24] M. Šuljić. "ALPIDE: the Monolithic Active Pixel Sensor for the ALICE ITS upgrade". In: *Journal of instrumentation* 11.11 (2016), pp. C11025–C11025. ISSN: 1748-0221. DOI: `10.1088/1748-0221/11/11/C11025`.

[25] Gianluca Aglieri Rinella. "The ALPIDE pixel sensor chip for the upgrade of the ALICE Inner Tracking System". In: *Nuclear instruments methods in physics research. Section A, Accelerators, spectrometers, detectors and associated equipment* 845 (2017), pp. 583–587. ISSN: 0168-9002. DOI: `10.1016/j.nima.2016.05.016`.

[26] Mager, Magnus. *MAPS in ALICE and perspectives.* Presented at the 4th FCC Physics and Experiments workshop. 2020.

[27] ALICE ITS ALPIDE development team. *ALPIDE Operations Manual.* `http://sunba2.ba.infn.it/MOSAIC/ALICE-ITS/Documents/ALPIDE-operations-manual-version-0_3.pdf`. Version: 0.3. 2016.

[28] Grøttvik, Ola. *pRU Data Format Specification.* `https://wiki.uib.no/pct/img_auth.php/c/c3/Data_format_v0.2.pdf`. 2018.

[29] J. Alme et al. "Performance of a digital calorimeter based on the ALPIDE pixel chip". Unpublished.

[30] D Malain and P Kanchana. "Evaluation of radiation safety for ionization chamber smoke detectors containing Am-241". In: *Journal of Physics: Conference Series* 1285 (Aug. 2019), p. 012047. DOI: `10.1088/1742-6596/1285/1/012047`.

[31] NIST. *ASTAR: Stopping Power and Range Tables for Alpha Particles.* `https://physics.nist.gov/cgi-bin/Star/ap_table.pl`. 2020.

[32] Yokoyama, Hiroki. *Test beam performance of a digital pixel calorimeter.* Presented at the TIPP 2021 conference. 2021.

[33]   Rogoschinski, Tim. *Simulation of a SiW pixel calorimeter*. Presented at the TIPP 2021 conference. 2021.

[34]   NIST. *ESTAR : Stopping Power and Range Tables for Electrons*. `https://physics.nist.gov/cgi-bin/Star/e_table.pl`. 2020.

[35]   Weaver, B. A. *dE/dx Calculator — Ionization Energy Loss*. `https://www.thedreamweaver.org/crange/recalc.html`. 2021.